Available online at www.sciencedirect.com

ScienceDirect

Geochimica et Cosmochimica Acta 148 (2015) 457–476

Geochimica et Cosmochimica Acta

www.elsevier.com/locate/gca

Discriminating secondary from magmatic water in rhyolitic matrix-glass of volcanic pyroclasts using thermogravimetric analysis

Thomas Giachetti [a,*], Helge M. Gonnermann [a], James E. Gardner [b], Thomas Shea [c], Andrew Gouldstone [d]

[a] Department of Earth Science, Rice University, Houston, TX, USA
[b] Jackson School of Geosciences, University of Texas, Austin, TX, USA
[c] Department of Geology and Geophysics, SOEST, University of Hawaii, Honolulu, HI, USA
[d] Department of Mechanical and Industrial Engineering, Northeastern University, Boston, MA, USA

Received 3 February 2014; accepted in revised form 18 October 2014; available online 27 October 2014

Abstract

Pyroclasts from explosive eruptions, such as the 1060 CE explosive Glass Mountain eruption of Medicine Lake volcano, California, contain large amounts of water. This may be the consequence of diffusive rehydration of the volcanic glass by meteoric (secondary) water after the eruption. Discriminating between magmatic and secondary water in the matrix glass of pyroclasts is important, because the degassing of magmatic water affects the intensity of volcanic eruptions. Such discrimination has remained a challenging problem, especially because some aspects of water diffusion in silicate glasses at low temperatures and atmospheric pressure remain poorly constrained. We used thermogravimetry to analyze the loss of water from natural volcanic glasses and glasses that were hydrated in the laboratory at magmatic temperatures and pressures. Numerical modeling of diffusive water loss during thermogravimetric analyses accounted for the interconversion of molecular water (H_2O_m) and hydroxyls groups (OH), and indicates that Glass Mountain pumices contain 0.2–0.5 wt% primary water, but gained 1–2 wt% of meteoric water by diffusive rehydration during the past 950 years. These results confirm that the majority of magmatic water is lost from the magma during explosive eruptions. Furthermore, the integration of thermogravimetric analysis and numerical modeling facilitates discrimination between the magmatic and secondary water content of volcanic glasses.

1. INTRODUCTION

The style and intensity of volcanic eruptions are largely controlled by the degassing of magmatic volatiles during magma ascent to the surface (e.g., Sparks, 1978, 2003; Eichelberger, 1995; Gonnermann and Manga, 2007). Among the different volatiles produced during volcanic eruptions, water is in many cases the most abundant. It is also the most important volatile species for the eruption of intermediate to felsic magmas, because of its influence on magma rheology and, thereby, on the dynamics of eruptive magma ascent (e.g., Shaw, 1972; Dingwell et al., 1996; Richet et al., 1996; Giordano and Dingwell, 2003).

Typically, the amount of water dissolved in an aliquot of melt, some of which may be preserved as dissolved water within the volcanic glass upon eruption and quenching, continuously decreases as the eruption proceeds. During ascent, the ambient pressure exerted on the magma

* Corresponding author.
E-mail address: thomas.giachetti@rice.edu (T. Giachetti).

http://dx.doi.org/10.1016/j.gca.2014.10.017
0016-7037/

decreases and, because of pressure-dependent water solubility, the melt becomes supersaturated in dissolved water, resulting in the nucleation and growth of bubbles of a supercritical water-bearing fluid phase (e.g., Hurwitz and Navon, 1994; Thomas et al., 1994; Lyakhovsky et al., 1996; Proussevitch et al., 1998; Gardner et al., 1999, 2000; Cashman, 2004; Gonnermann and Manga, 2007). Consequently, during eruptive magma ascent the concentration of dissolved water decreases and in principle the erupting magma may be almost 'dry' when it reaches the Earth's surface.

Recent work by Gonnermann and Houghton (2012) suggested that this may not necessarily be the case. Detailed modeling of magma degassing during Episode III of the 1912 Plinian eruption of Novarupta volcano, Alaska, indicated the possibility that the magma could have retained a significant fraction of its pre-eruptive water as dissolved water within the melt, due to disequilibrium degassing. Instead, the magma may have lost a large fraction of its dissolved water by open-system degassing shortly before or after fragmentation (e.g., Namiki and Manga, 2008), or the melt may have retained several weight percent of dissolved water upon quenching. Total water contents in the matrix glass of pyroclasts from the 1912 Novarupta eruption are approximately 2–3 wt% (Giachetti and Gonnermann, 2013), perhaps consistent with incomplete degassing of the erupting magma, but contrary to the magma losing most of its water upon ascent to the surface (e.g., Jaupart and Allègre, 1991; Gardner et al., 1996).

Alternate explanations for the surprisingly high water content of pyroclasts from the 1912 Novarupta eruption, as well as in pyroclasts from other explosive eruptions of silica-rich magmas (Giachetti and Gonnermann, 2013), could be bubble resorption (e.g., Westrich and Eichelberger, 1994; Yoshimura and Nakamura, 2008, 2010; Watkins et al., 2012; McIntosh et al., 2014), interaction of the ascending magma with hydrothermal fluids or ice (e.g., Burnham, 1979; Villemant and Boudon, 1999; Tuffen et al., 2010), or the gradual diffusion of meteoric water into the volcanic glass after eruption and deposition (e.g., Ross and Smith, 1955; Friedman et al., 1966; Friedman and Long, 1976; Newman et al., 1986; Denton et al., 2009, 2012; Giachetti and Gonnermann, 2013). The latter is referred to as 'rehydration'. Upon rehydration, the fraction of dissolved water that does not represent pre-eruptive magmatic ('primary') water is often referred to as 'secondary' water. Obviously, the ability to discriminate between magmatic and secondary water is of critical importance to understanding the dynamics that govern explosive volcanic eruptions. For example, quantifying the relative proportion of magmatic and secondary water would help to further constrain the relative degrees of pre- vs. post-fragmentation magma open-system degassing and, hence, the conditions at magma fragmentation.

The discrimination between magmatic and secondary water in the matrix glass of pyroclasts is the objective of our study. Although several different methods to distinguish primary from magmatic water exist (e.g., Tuffen et al., 2010), each has significant limitations. For example, the D/H ratio of meteoric water is distinct from magmatic water (e.g., DeGroat-Nelson et al., 2001; Harford et al., 2003; Tuffen et al., 2010). However, Nolan and Bindeman (2013) showed that the D/H ratio can be rapidly changed by minor diagenesis, even at relatively low temperatures of 20 °C (and despite no significant water gain after 2 years at 70 °C was observed), making its interpretation complicated. Among the different methods available to distinguish magmatic from secondary water, oxygen isotopes may be the most reliable technique (Goff and McMurtry, 2000; Tuffen et al., 2010; Nolan and Bindeman, 2013). Here we focus on alternate method: Thermogravimetric analysis (TGA). During TGA a sample is heated (in this case at atmospheric pressure) to a specified temperature and at a specified rate, while its change in mass is continuously recorded (e.g., Eichelberger and Westrich, 1981; Roulia et al., 2006; Anovitz et al., 2008; Denton et al., 2009, 2012; Stevenson et al., 2009; Applegarth et al., 2013). Because the solubility of water in silicate glasses at atmospheric pressure decreases during heating, water diffuses out of the sample during TGA. The discrimination between magmatic and secondary water is based on the hypothesis that secondary water is more 'weakly bound' within the silica network than magmatic water, and that it is therefore lost from the sample at lower temperatures (Newman et al., 1986; Westrich, 1987; Roulia et al., 2006; Denton et al., 2009, 2012). We performed a series of TGA experiments of rhyolitic glasses, which were hydrated at known and controlled conditions in the laboratory (magmatic pressures and temperatures) and, thus, of known magmatic water content. Subsequent modeling of water loss during TGA allowed us to establish a framework for quantifying magmatic water content and its application to pumices from explosive volcanic eruptions.

2. WATER IN RHYOLITIC MELT AND GLASS

In this section we summarize the key points on speciation, solubility and diffusivity of water in rhyolitic melts and glasses. We refer to the reviews by Zhang et al. (2007) and Zhang and Ni (2010) for further information.

2.1. Speciation

Water dissolves in silicate melts as molecular water (H_2O_m) and hydroxyls (OH). The total amount of dissolved water is denoted as H_2O_t and herein sometimes referred to as water. Both H_2O_m and OH can be quantified using infrared and Raman spectroscopy (e.g., Stolper, 1982b; Ihinger et al., 1994; Cherniak et al., 2010; Ni et al., 2013). H_2O_m and OH can interconvert through the reaction (e.g., Stolper, 1982a,b)

$$H_2O_m + O \rightleftharpoons 2\ OH, \tag{1}$$

where O is an anhydrous oxygen ion and the ionic charge is not shown. The equilibrium constant of Eq. (1) can be written as

$$K = \frac{[OH]^2}{[H_2O_m][O]}, \tag{2}$$

Table 1
Symbols used in this study and their units with description. In the text, H_2O_t, H_2O_m and OH refer to total water, molecular water and hydroxyls groups, respectively.

Symbol	Unit	Description
A		Absorbance at the corresponding wavelength (FTIR)
C	wt%	Concentration of the different species
d	cm	Sample's thickness where the spectrum is collected (FTIR)
D	$m^2\,s^{-1}$	Diffusivity of a species
k'_f	s^{-1}	Forward reaction rate coefficient
k'_b	s^{-1}	Backward reaction rate coefficient
K		Equilibrium constant of the speciation reaction
L	m	Characteristic diffusion length
M	%	Sample mass loss relative to the initial mass of the sample
P	Pa	Pressure
r	m	Radial coordinate
R	m	Grain radius
t	s	Time
T	K	Temperature
X	mole fraction	Mole fraction of a species on a single oxygen basis
ε	$l{\cdot}mol^{-1}{\cdot}cm^{-1}$	Linear molar absorption coefficient (FTIR)
ρ	$g{\cdot}cm^{-3}$	Density of the rhyolitic glass
τ_{D_m}	s	Characteristic time for diffusion of molecular water
τ_ξ	s	Characteristic time for speciation reaction
τ_T	s	Characteristic time for heating of the TGA run
ξ	mole fraction	Reaction progress parameter

where brackets mean activities (see Table 1 for a list of symbols). Activities are approximated by mole fractions, X, and calculated as (Zhang and Ni, 2010)

$$X_{H_2O_t} = \frac{\frac{C_{H_2O_t}}{18.0152}}{\frac{C_{H_2O_t}}{18.0152} + \frac{100 - C_{H_2O_t}}{32.49}}, \quad (3)$$

$$X_{H_2O_m} = \frac{C_{H_2O_m}}{C_{H_2O_t}} X_{H_2O_t}, \quad (4)$$

$$X_{OH} = 2(X_{H_2O_t} - X_{H_2O_m}), \quad (5)$$

$$X_O = 1 - X_{H_2O_m} - X_{OH}, \quad (6)$$

where C (wt%) is the mass concentration of the different species in the melt (glass).

The equilibrium speciation in rhyolitic melt (Eq. (2)) has been extensively investigated over the last decades (e.g., Newman et al., 1986; Zhang et al., 1997a; Withers and Behrens, 1999; Hui et al., 2008; Zhang and Ni, 2010, and references therein) and a frequently used speciation model is given by Zhang et al. (1997a)

$$K = \exp\left(1.876 - \frac{3110}{T}\right), \quad (7)$$

where T (Kelvin) is the temperature. The effect of pressure on speciation is not very large (Hui et al., 2008) and usually not taken into account. Eqs. (1)–(7) show that OH is the dominant species at low H_2O_t, whereas H_2O_m becomes the dominant species when H_2O_t reaches several wt% (e.g., ≈5 wt% at a temperature of 620 °C; see Fig. 3 of Zhang and Ni (2010), for another example).

2.2. Water solubility

The solubility of water in rhyolitic melt (glass) is a function of pressure and temperature and is well known in the range of 650–1200 °C and 0–3 GPa (e.g., Goranson, 1931; Friedman et al., 1963; Shaw, 1974; Holtz et al., 1995; Moore et al., 1995; Gardner et al., 1999; Liu et al., 2005; Zhang et al., 2007; Duan, 2014). Because of the time required to perform (de)hydration experiments at low temperatures, where water diffuses very slowly, the solubility of water in rhyolitic glass at temperatures below 650 °C remains poorly constrained. The few existing experiments at atmospheric pressure and 200 °C suggest that water solubility is approximately 2–3 wt% (Anovitz et al., 2008), the solubility therefore increases with decreasing temperature. Denton et al. (2009, 2012) measured water contents of up to 4 wt% in non-altered hydrated obsidians, whereas Lee et al. (1974) and Jezek and Noble (1978) found values of up to 7 wt%, and Anovitz et al. (1999) measured values of up to 10 wt%. Water contents in non-altered pumiceous pyroclastic deposits have been found to reach values of up to 5 wt% (Denton et al., 2009; Giachetti and Gonnermann, 2013, and references therein).

2.3. Diffusivity

2.3.1. Diffusivity above 400 °C

The dependence of water diffusivity on temperature and water content is well constrained above 400 °C, (see Zhang and Ni, 2010, and references therein). In silicate melt (glass), H_2O_m is assumed to be the only diffusing species, because the diffusion of OH is several orders of magnitude slower and, therefore, usually assumed negligible (Zhang et al., 1991; Zhang and Ni, 2010). However, Ni et al. (2013) have recently shown that the ratio $D_{OH}/D_{H_2O_m}$ can reach 0.2 in haploandesitic melt at temperatures between ≈1350 and 1570 °C and H_2O_t content close to zero. Therefore, it remains uncertain whether OH diffusion is negligible or not at high temperatures and low H_2O_t.

Ni and Zhang (2008) obtained the following equation for the diffusivity of molecular water in rhyolitic glass, by combining the experimental data of Zhang et al. (1991, 2000) with new measurements,

$$D_{H_2O_m} = e^{\alpha}, \quad (8)$$

where

$$\alpha = -14.26 + 1.888P - 37.26X_{H_2O_t} - \frac{12,939 + 3626P - 75,884X_{H_2O_t}}{T}. \quad (9)$$

Here P (GPa) is the pressure, $X_{H_2O_t}$ is the mole fraction of total water and $D_{H_2O_m}$ is in $m^2 \cdot s^{-1}$. This model is valid for 403–1629 °C, 0–1.9 GPa and 0.1–7.7 wt% of H_2O_t.

2.3.2. Diffusivity below 400°C

Similar to solubility, water diffusivity in rhyolite at low pressures and temperatures is poorly constrained. The existing data on water diffusivity in rhyolitic glass below 400°C are mostly based on obsidian hydration dating (see Liritzis and Laskaris, 2011, and references therein) and are scattered over almost four orders of magnitude, with no self-consistent formulation that can explain these variations (see Table 2 in Giachetti and Gonnermann, 2013, for a compilation). The data, however, suggest that water may diffuse faster at atmospheric temperatures (approx. 0–40°C) than expected from the extrapolation of Eq. (8) to lower temperatures (e.g., Anovitz et al., 2008; Giachetti and Gonnermann, 2013).

3. METHODOLOGY

The different steps of our experiments are summarized in Fig. 1 and described in the following paragraphs.

3.1. Sampling

We collected obsidian blocks on the carapace of the 1060 CE Glass Mountain rhyolitic flows of Medicine Lake volcano, California (e.g., Anderson, 1933; Heiken, 1978; Nathenson et al., 2007; Donnelly-Nolan et al., 2008) for use as starting material for our experiments. Attention was paid to collect glassy blocks with no obvious banding or vesicles. The Glass Mountain obsidian samples collected contain on average approximately 3 vol% of microlites (Stevenson et al., 1996) and are rhyolitic in composition, with a SiO_2 content of approximately 72–75 wt% (Anderson, 1933; Tatlock et al., 1976; Heiken, 1978; Grove and Donnelly-Nolan, 1986; Grove et al., 1997). The density of the obsidian, measured by He-pycnometry, is 2.43 ± 0.05 g·cm^{-3}, consistent with the 2.45 g·cm^{-3} measured by Tatlock et al. (1976). The water content of the collected obsidian is <0.5 wt% (e.g., Eichelberger and Westrich, 1981; DeGroat-Nelson et al., 2001; Castro et al., 2005), and the content in volatiles other than water is negligible, with CO_2, HF and HCl altogether accounting for <3% of the total volatile content (Eichelberger and Westrich, 1981), and CO_2 content is also negligible (Anderson,1933).

3.2. Electronic microprobe (EMP)

Analyses of major elements and Cl, F, S within some of the pre- and post-TGA glasses were obtained using a JEOL Hyperprobe JXA-8500F to (1) verify chemical homogeneity of the samples, and (2) characterize potential contributions of volatiles other than water to the TGA mass loss curves. Analyses were performed using a 15 keV accelerating voltage, 10 nA beam current, 10 µm beam diameter, and peak and background counting times of 20 s (Na, Si), 30 s (Al, Ti, Mg, Mn, Fe, P, S, Cl), 50 s (Ca), 60 s (K), and 120 s (F). Two natural glasses (V-72, V-56, Jarosewich et al., 1980) as well as mineral standards were used for calibration. Glass standards were analyzed repeatedly to monitor any possible drift. Relative precision was on average 0.5%

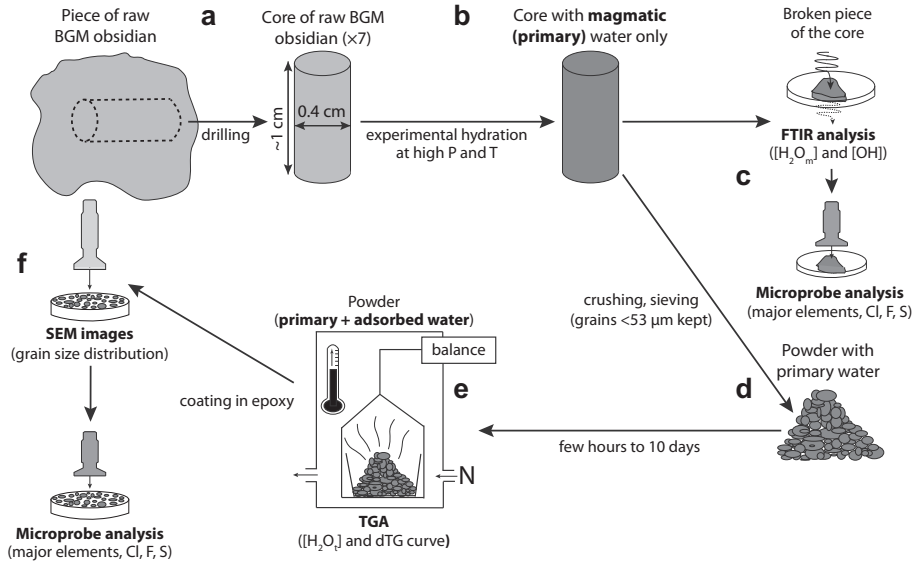

Fig. 1. Summary of the experimental steps of our study. (a) Seven cores were drilled from a single piece of Glass Mountain obsidian. (b) The cores were experimentally hydrated for 38–148 h at 4–160 MPa and 850–1150 °C, in order to produce rhyolitic glasses with different amounts of primary water. (c) An aliquot of each core was analyzed by FTIR to obtain water concentration and speciation and by EMP to obtain major and volatiles elements. (d) The remainder of the core was crushed and sieved, with grains <53 µm kept for TGA analysis. (e) Samples were analyzed by TGA from room temperature to 1000 °C at a rate of 20 °C·min^{-1}. During the time between the crushing and TGA (hours to days), the powder adsorbed small amounts of atmospheric water. (f) The powder G-1226 was coated in epoxy, images were taken by SEM, and the grain size distribution was obtained using the ImageJ software.

for SiO_2, CaO and Al_2O_3, 1–1.5% for MgO, FeO, Na_2O, K_2O, 4% for TiO_2, 10% for MnO, Cl, and 15% for S, F and P_2O_5 based on repeated standard analyses. Four to six spot analyses were collected in each sample, at several tens of microns from each other, in order to obtain a rough estimate of compositional glass homogeneity.

3.3. Experimental hydration at high temperatures and pressures

The goal of the experimental hydration was to synthesize homogeneous glass with different amounts of primary water. Cores of 1 cm in length, 0.4 cm in diameter, and weighing 100–150 mg were drilled several centimeters below the surface of a single large block of obsidian (Fig. 1a). Each core was placed inside an Au–Pd capsule, together with 1–12 mg of deionized water. The capsule was then welded shut, and weighed to check that no water was lost during the weld. Experiments were run for 46 to 148 h at pressures between 4 and 160 MPa and temperatures between 850 and 1150 °C (see Table 2 for experimental conditions). For the experiment run at <900 °C the capsule was placed inside an externally heated, cold-seal pressure vessel, made of a Nickel-based alloy. Each sample was pressurized using water, and the oxygen fugacity of the experiment was maintained near that of the Ni–NiO buffer reaction by the use of a Ni filler rod inside the pressure vessel. The samples were quenched by removing the pressure vessel from the furnace and, after blowing on the vessel with compressed air, immersing it in a bucket of water. In this manner each sample was completely cooled to room temperature in less than one minute. For experiments at >900 °C the capsules were placed inside externally heated TZM pressure vessels, which are pressurized with argon and hung inside of a box furnace. A few bars of methane were added to the argon, in order to minimize hydrogen loss from the capsules. Samples were quenched by pulling the pressure vessel out of the furnace and inverting it, causing the capsule to drop to the water-cooled jacket at the end of the pressure vessel. In this case, pressure was maintained during the cooling to room temperature. After quenching, each sample consisted of a solid piece of hydrated glass, containing a certain amount of dissolved magmatic water (Fig. 1b). Some samples lost weight during the experiment and were probably not fully saturated at experimental conditions, but the resultant glasses were nevertheless useable because the water content, its spatial distribution, as well as speciation were measured by Fourier-Transform Infrared spectroscopy (FTIR) prior to TGA.

Table 2
Experimental conditions.

Sample	P (MPa)	T (°C)	duration (h)
G-1290	4	1150	48
G-1298	12	1100	48
G-1299	42	1100	47
G-1380	12.7	1050	87
G-1300	81	1100	46
G-1186	160	1000	110
G-1226	150	850	148

3.4. Fourier-Transform Infrared spectroscopy

The water content of each sample, as well as water speciation, were measured by FTIR in transmittance mode on doubly polished wafers, using a Thermo Electron Nicolet 6700 spectrometer and Continuμm IR microscope (Fig. 1c). Depending on sample total water content, spectra were collected for each sample either using 250 scans at a resolution of 4 cm^{-1} in the near-IR region (3800–7800 cm^{-1}) with a CaF_2 beamsplitter and white light, or using 100 scans in the mid-IR region (800–4000 cm^{-1}) with a KBr beamsplitter and IR light. For samples with less than 1 wt% of water, H_2O_t and H_2O_m contents were measured from absorbances at 3550 and 1630 cm^{-1}, respectively, while for higher water contents, H_2O_m and OH contents were determined from absorbances at 5250 and 4500 cm^{-1}, respectively. In all cases, the baseline used was either a straight line if the background was flat, or a French curve if the background was curved. The concentration of each species was determined using the Beer–Lambert law

$$C = \frac{18.02 \times 10^2 A}{\rho \, \epsilon \, d}. \quad (10)$$

Here C (wt%) is the concentration of the absorbing species, A is the absorbance at the corresponding wavelengths (peak height in dimensionless absorbance units), ρ is the density of the glass (2.43 ± 0.05 g·cm^{-3}), d (cm) is the sample's thickness where the spectrum is collected, and ϵ (l·mol^{-1}·cm^{-1}) is the linear molar absorption coefficient at the considered wavelength. For rhyolite at 1630, 3550, 4500 and 5250 cm^{-1}, absorption coefficients are 55 ± 2 (Newman et al., 1986), 75 ± 4 (Okumura et al., 2003), 1.42 ± 0.12 and 1.75 ± 0.08 l·mol^{-1}·cm^{-1} (Okumura and Nakashima, 2005), respectively. The sample thickness at the locations where the spectra were collected (cf. Table 4) was measured by focusing on the top and bottom of a sample with a petrographic microscope and measuring the distance between those positions, using a Heidenhain focus drive linear encoder. The average error for each thickness, determined by repeatedly focusing through a sample, was 3.8% relative at a maximum. For each measurement, the relative error on the total water content, obtained from the propagation of the errors associated with the four different parameters of Eq. (10) is ±6–17%. Applying the method of Zhang et al. (1997b) to treat the data gave results that were always within those obtained using Eq. (10).

3.5. Particle size distribution

Following hydration the cores were crushed using a mortar and pestle and sieved so that all grains for TGA analysis had a size of <53 μm (Fig. 1d). This size range was chosen (1) to be similar to the thickness of the glass between neighboring vesicles in natural highly porous samples, which is the characteristic diffusion length for water during TGA and is of the order of microns (e.g., Klug and Cashman, 1996; Giachetti et al., 2010) and, (2) to avoid

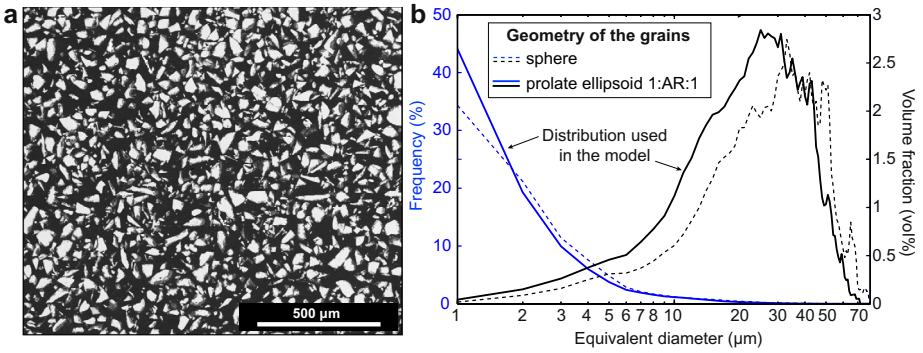

Fig. 2. (a) Backscattered electron image of a typical glass powder analyzed by thermogravimetry. (b) Grain size distribution obtained by image analysis (4183 grains analyzed), assuming that grains are either spherical (dotted lines) or 1:2.1:1 prolate ellipsoids (solid lines).

bubble nucleation and growth during TGA of the water-rich samples. We measured the particle size distribution of one powder (sample G-1226) by image analysis, and the other powders are assumed to present the same distribution, because they were prepared following the identical procedure. After the TGA run (see Section 3.7), the powder was embedded in resin, polished, and imaged using a Scanning Electron Microscope (Figs. 1f and 2a). The powder did not significantly sinter and fuse, because it was quickly cooled after the temperature had reached 1000 °C. Consequently, the grains were easily separated as demonstrated in Fig. 2a. The surface areas of 4183 grains, which were selected from the SEM images, were estimated using the imageJ software. The aspect ratio of the grains is on average 2.1, and we therefore assumed that the grains were 1:2.1:1 prolate ellipsoids for calculating the grain size distribution. The resulting distribution of particle volume fraction is negatively skewed with a peak centered at approximately 25 µm (Fig. 2b).

3.6. Water adsorption and rehydration

To avoid any loss of primary water, the powders were not dried or exposed to any heating procedure or chemical treatment before TGA analysis. Because the specific surface area of our glasses is very high (about 2.4 μm^{-1}), the grains may have been affected by atmospheric water during the time interval between crushing and TGA, which was typically few minutes to 10 days (Fig. 1e). As illustrated in Fig. 3, atmospheric/meteoric water may become adsorbed on the surface of any silicate glass (hereafter referred to as 'adsorbed water') and may also diffuse into the glass (i.e., 'secondary water').

Adsorption of atmospheric/meteoric water onto silicate glass has been described as a complex, multi-step process, leading to the rapid increase of the total amount of water carried by the sample (e.g., Razouk and Salem, 1948; Westrich, 1987; Garofalini, 1990; Delmelle et al., 2005; Christy, 2010). For example, the amount of adsorbed water reached 0.25 wt% in grains <44 µm after more than 100 days atmospheric exposure (Newman et al., 1986). The increase in adsorbed water with time is non-linear and the sample should be heated to temperatures far above 100 °C (even under vacuum), in order to remove all adsorbed water molecules (e.g., Kunkel, 1950; Newman et al., 1986; Delmelle et al., 2005). Our experimental glasses adsorbed atmospheric water before TGA, and we show in Section 4.4.1 that the amount of adsorbed water is restricted to few tenths of wt% at most and, furthermore, that it can be discriminated from primary water during TGA.

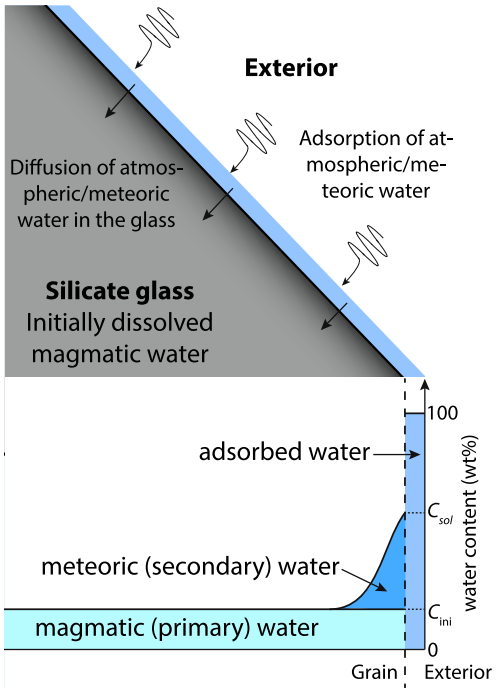

Fig. 3. Schematic diagram (not to scale) illustrating water adsorption and rehydration. A silicate glass with initially dissolved magmatic water (considered here homogeneous and equal to C_{ini} for simplicity) will adsorb water molecules when in contact with atmospheric or meteoric water, creating a film at the glass surface. During rehydration some of this adsorbed water then diffuses into the grain, forming a thin layer of secondary water directly beneath the glass surface, thereby increasing the total amount of dissolved water. The solubility of water in the glass at atmospheric conditions, C_{sol}, and its diffusivity will partly control the total amount of secondary water gained during rehydration.

Although not well constrained, the diffusivity of water in rhyolitic glass at room temperature is low, ranging between about 10^{-24} and 10^{-21} $m^2 \cdot s^{-1}$ (see Table 2 of Giachetti and Gonnermann, 2013). Consequently, during the short time interval between crushing and TGA, secondary water is expected to be confined to a 0.8–41 nm-thick layer beneath the grain surface. If the concentration in secondary water in this layer is uniformly equal to the solubility of water in rhyolitic glass at room temperature (poorly known but maybe around 3–4 wt%, see Section 2.2), the total amount of secondary water in our samples (grain size up to 53 μm) is expected to be of the order of 0.001–0.01 wt%, which is far below the error associated with TGA. It is thus reasonable to assume that secondary water is absent from our experimental glasses. Lastly, it should be noted that the glass may also have adsorbed CO_2 from the laboratory atmosphere, but this CO_2 will be liberated during TGA before the temperature reaches 100 °C (Leal et al., 1995).

3.7. Thermogravimetric analysis

TGA was performed using a TA Instruments Q500 Thermogravimetric Analyzer. Between 15 and 45 mg of the powder were placed inside a tared alumina cup and mounted on the thermogravimeter's sample beam. The powder was heated from room temperature to 1000 °C at a constant rate of 20 °C·min^{-1}. Concurrently the mass of the sample was measured at a frequency of 2 Hz. Throughout the analysis samples were purged by an oxygen-free nitrogen atmosphere with better than 99.999% purity and at 150 ml.min^{-1}. Because the content of volatiles other than water was negligible, the mass loss during TGA is approximately equal to the water loss. We confirmed that all volatiles were lost from the sample by performing a second TGA on several samples, during which no additional mass loss was observable. We performed three TGAs on 25 mg of dry alumina powder using the same procedure as for the samples. We then used these runs as blank measurements, as well as their repeatability to estimate the uncertainty associated with the total water content, which is approximately ±10%.

4. RESULTS

4.1. Measured major and volatiles elements composition

Table 3 shows the composition in major and volatile elements of the hydrated glasses obtained by EMP. All the glasses are homogeneous, with a SiO_2 of 74–75 wt% and overall compositions similar to those available in the literature (e.g., Anderson, 1933; Tatlock et al., 1976; Eichelberger and Westrich, 1981). The composition in major elements after TGA is the same as before TGA (within errors) and not shown here. The volatiles contents of the glasses before and after TGA analysis are almost identical, with Cl around 500–800 ppm, S up to 100 ppm and F below the detection limit (around 200 ppm), showing that the contribution of these three volatile phases in the mass loss of the glasses during TGA is negligible.

4.2. Measured water contents and speciation

Dissolved water contents obtained by TGA and FTIR, as well as the speciation data measured by FTIR, are listed in Table 4. FTIR data show that all samples are homogeneous, the spatial variability in water content and speciation being lower than the error associated with the measurement. The total water contents range between approximately 0.3 wt% in sample G-1290 and 4.4 wt% in sample G-1226. The speciation data are consistent with the literature, in that OH is the dominant species at total water contents of <0.5 wt%, whereas H_2O_m is the dominant species in the water-rich samples. Total water content, $[H_2O_t]$, obtained by TGA ranges approximately from 0.4 wt% in sample G-1290 to 5.2 wt% in sample G-1226, and are for most samples a few tenths of a weight % higher

Table 3
EMP data of the experimentally hydrated cores. Values are in wt%, unless indicated. Numbers in parentheses indicate standard deviation within the 4 to 6 data points collected for each sample. F was measured but below the detection limit for all the samples.

	G-1290	G-1298	G-1299	G-1300	G-1226
SiO_2	74.90(0.36)	74.48(0.16)	73.86(0.22)	74.62(0.27)	74.79(0.09)
TiO_2	0.26(0.04)	0.25(0.03)	0.28(0.04)	0.27(0.02)	0.25(0.04)
Al_2O_3	14.24(0.11)	13.94(0.10)	13.95(0.08)	14.16(0.21)	14.00(0.03)
FeO	1.74(0.05)	1.57(0.06)	1.61(0.15)	1.69(0.03)	1.27(0.05)
MnO	0.04(0.03)	0.02(0.02)	0.04(0.02)	0.03(0.01)	0.03(0.02)
MgO	0.29(0.02)	0.25(0.01)	0.27(0.02)	0.29(0.01)	0.26(0.01)
CaO	1.30(0.02)	1.26(0.04)	1.19(0.02)	1.30(0.03)	1.28(0.02)
Na_2O	3.82(0.06)	3.96(0.06)	3.89(0.09)	3.86(0.03)	3.62(0.11)
K_2O	4.32(0.03)	4.43(0.02)	4.32(0.04)	4.30(0.04)	4.38(0.02)
P_2O_5	0.03(0.02)	0.04(0.03)	0.04(0.02)	0.02(0.02)	0.04(0.02)
			Before TGA		
S (ppm)	31(54)	17(37)	19(42)	32(72)	102(165)
Cl (ppm)	551(194)	723(120)	525(152)	764(89)	637(159)
			After TGA		
S (ppm)	–	0(0)	35(67)	–	95(103)
Cl (ppm)	–	656(72)	706(155)	–	561(82)

Table 4
FTIR and TGA data obtained on the experimentally hydrated samples. The density of the rhyolitic glass, measured by He-pycnometry, is 2.43 ± 0.05 g·cm^{-3}. The absorption coefficients used are $\epsilon_{1630} = 55 \pm 2$ (Newman et al., 1986), $\epsilon_{3550} = 75 \pm 4$ (Okumura et al., 2003), $\epsilon_{4500} = 1.42 \pm 0.12$ and $\epsilon_{5230} = 1.75 \pm 0.08$ l·mol^{-1}·cm^{-1} (Okumura and Nakashima, 2005). Concentrations are given in wt%. Numbers in parentheses for the thickness and absorbances are the standard deviations of the *n* spectra. The variation in $[H_2O_m]$, $[H_2O_t]$ and [OH] within each glass is always lower than the error associated with each FTIR data, obtained by propagating the error on the absorbance, absorption coefficient, thickness and density.

	G-1290	G-1299	G-1298	G-1380	G-1300	G-1186	G-1226
n	1	10	10	10	8	3	8
Thickness	318(–)	453(6)	168(29)	395(53)	262(9)	303(20)	258(17)
A_{1630}	0.155(–)	0.141(0.032)	0.158(0.031)	0.760(0.000)	–	–	–
A_{3550}	0.960(–)	1.925(0.057)	0.658(0.101)	1.903(0.206)	–	–	–
A_{4500}	–	–	–	–	0.036(0.002)	0.096(0.001)	0.078(0.010)
A_{5230}	–	–	–	–	0.052(0.001)	0.152(0.006)	0.171(0.016)
$[H_2O_m]$	0.07 ± 0.01	0.04 ± 0.01	0.13 ± 0.01	0.26 ± 0.03	0.59 ± 0.07	2.12 ± 0.15	2.81 ± 0.24
[OH]	0.23 ± 0.05	0.38 ± 0.03	0.27 ± 0.05	0.22 ± 0.09	1.03 ± 0.15	1.66 ± 0.19	1.57 ± 0.21
$[H_2O_t]_{FTIR}$	0.30 ± 0.04	0.42 ± 0.04	0.40 ± 0.04	0.49 ± 0.06	1.62 ± 0.22	3.78 ± 0.35	4.38 ± 0.45
$[H_2O_t]_{TGA}$	0.42 ± 0.04	0.78 ± 0.08	0.74 ± 0.08	0.70 ± 0.07	1.65 ± 0.17	4.00 ± 0.40	5.24 ± 0.52

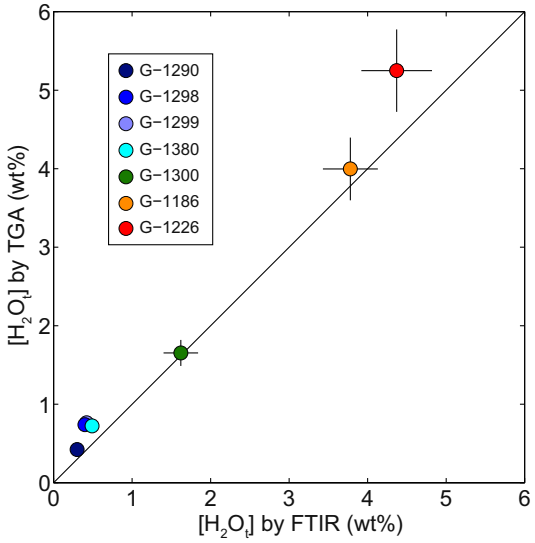

Fig. 4. Comparison of the concentration of water, $[H_2O_t]$, measured by TGA and by FTIR (corresponding values provided in Table 4). We attribute the slightly higher water contents measured by TGA predominantly to the adsorption of atmospheric water.

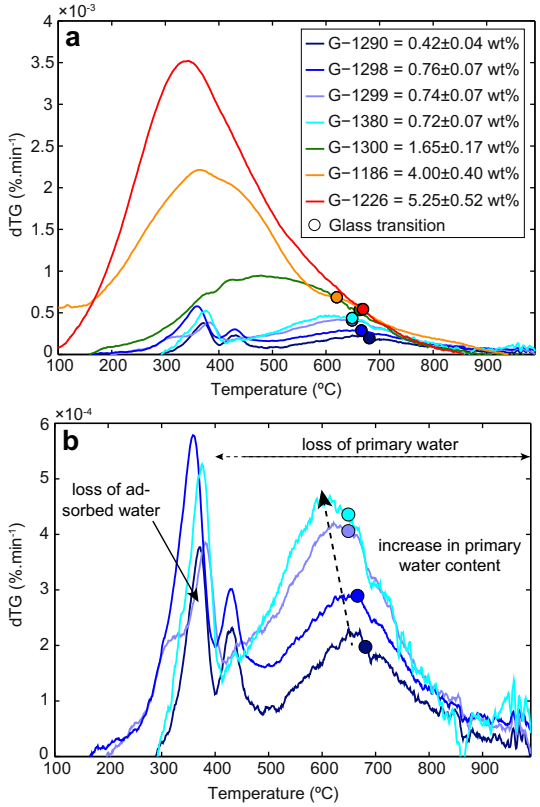

Fig. 5. (a) Rate of mass loss (dTG) as a function of temperature, *T*, for the experimentally hydrated glasses. Total mass loss is indicated in the legend. (b) Subset of samples shown in (a) with an enlarged vertical scale (dTG axis). The filled circles indicate where each sample passes through the glass transition (Deubener et al., 2003). Samples with less than approximately 0.5 wt% water (G-1290, G-1298, G-1299, G-1380) have multiple peaks. For those samples, we interpret the two peaks at <480 °C as the loss of adsorbed water, whereas the peaks at >600 °C are consistent with the loss of magmatic water. Samples with more than approximately 0.5 wt% water (G-1300, G-1186, G-1226) exhibit a single mass-loss peak, because the loss of magmatic water is shifted to lower temperatures, due to high water diffusivity, and overlaps with the loss of adsorbed water.

than those measured by FTIR, but without any systematic correlation with $[H_2O_t]$ (Fig. 4).

4.3. Measured mass loss during TGA

In the following, the percentage of sample mass loss relative to the initial mass of the sample is called *M*. TGA results are usually plotted as the first derivative of *M* with respect to time, that is dM/dt (%·min^{-1}), and the resulting curve, when plotted at a function of *T*, is called the dTG curve. Therefore, a peak in dTG indicates when the rate of mass loss has reached a maximum, and is usually a consequence of temperature-dependent solubility, speciation and/or diffusivity. Fig. 5 shows the dTG curves of all seven

experiments. For samples with water contents of less than approximately 0.5 wt% there are typically three peaks: a narrow peak centered at approximately 360 °C, a narrow peak centered at approximately 430 °C, and a broad peak centered at approximately 650 °C. For samples with greater than approximately 0.5 wt% of water, the first two peaks overlap, forming a somewhat broader peak. The filled circle on Fig. 5 denotes the glass transition temperature, calculated following Deubener et al. (2003), while taking into account the loss of water with increasing temperature. For samples with less than approximately 0.5 wt% of water, the glass transition coincides with the second peak, whereas for more water-rich samples, most of the water is lost before the sample reaches the glass transition temperature.

4.4. Interpretation of measurements

4.4.1. Adsorbed water

We speculate that the difference between the total water content, as measured by TGA and FTIR, is a consequence of atmospheric water adsorption of vapor on the surface of the glass grains, and furthermore, that this adsorbed water is lost around 400 °C during TGA. Describing the complex adsorption of water before TGA and its desorption during TGA is beyond the scope of this study. Adsorbed water consists of layers of water molecules that are attached to the glass surface, the first layer being bonded to the grain via Si-O bonds and subsequent layers of water molecules being attached through a network of hydrogen bonds between individual water molecules (e.g., Garofalini, 1990; Christy, 2010; Nolan and Bindeman, 2013). It has already been shown that during TGA the loss of adsorbed water occurs at lower temperatures than the loss of magmatic water, mainly because of its geometrical position on the external surface of each grain and its speciation (e.g., Newman et al., 1986; Westrich, 1987; Sodeyama et al., 1999; Roulia et al., 2006). The temperature at which adsorbed water will be lost depends mainly on the heating rate. Sodeyama et al. (1999) found that adsorbed water loss from obsidian powder, during TGA at 20 °C·min^{-1}, occurs at 300–400 °C and around 280 °C during TGA at 5 °C·min^{-1}. During stepwise pyrolysis adsorbed water may be lost at or below approximately 200 °C (Newman et al., 1986; Westrich, 1987). Consistent with these results, adsorbed water was lost during our analyses at 360–430 °C, as manifested by the first dTG peaks centered around 360–430 °C, which suggest an almost invariant characteristic 'loss' time.

4.4.2. Magmatic water

During sample hydration the dissolved (magmatic, primary) water speciated and the resultant H_2O_m and OH were homogeneously distributed within the glass, as confirmed by FTIR. The characteristic diffusion length for magmatic water scales as the grain radius, which is several orders of magnitude larger than the layer of adsorbed water on the grain surface. However, because water diffusivity substantially increases with water content (see Eqs. (8) and (9)), the dTG peak corresponding to magmatic water shifts in position toward lower temperatures with increasing water content. In our experiments the shift was from 660 °C for 0.3 wt% H_2O_t down to 360 °C for 4.4 wt% H_2O_t (Fig. 5). In addition, at high H_2O_t the peak becomes much larger in amplitude and width than the adsorbed water peak, thus masking the latter's presence.

5. NUMERICAL MODELING OF WATER LOSS DURING TGA

We use a numerical model of coupled water diffusion and speciation to reproduce the measured dTG profiles. This facilitates an improved quantitative interpretation of the TGA experiments. The following paragraphs provide details about the numerical modeling.

5.1. Conceptual model

We assume that each sample can be approximated by a finite distribution of spherical rhyolitic glass grains. Consistent with the FTIR measurements, each grain is assumed to be initially homogenous in magmatic water content, and with relative proportions of H_2O_m and OH equal to the values measured by FTIR (cf. Table 4). Although individual grains are not of perfectly spherical shape, we believe that the difference between modeling a grain with the measured aspect ratio of 2.1:1 and approximating it as a spherical grain does not significantly affect our model results (see Appendix C for an analysis of model sensitivity on geometry). The change in mass during gradual heating of the sample is modeled through a coupled reaction-diffusion calculation. Both the temperature- and water concentration-dependent diffusion of H_2O_m and OH (Eqs. (8) and (9)), as well as the temperature- and water-dependent interconversion between OH and H_2O_m (Eq. (1)), are modeled for individual grains of different size. Each such modeled grain is representative of a certain size fraction of grains, corresponding to the measured distribution of grain sizes. The total change in mass is then calculated as the change in mass of each representative grain, multiplied by the number of grains of that size interval within the sample. Because the characteristic time scale for thermal diffusion ($\sim 10^{-4}$ s), using thermal diffusivities of Bagdassarov and Dingwell (1994), is significantly lower than the characteristic time for heating during TGA ($\sim 10^{3}$ s), each grain will be near thermal equilibrium throughout the experiment. We therefore assume that each sample grain is always at a uniform temperature equal to the measured temperature inside the thermogravimeter chamber at the given time.

5.2. Governing equations

The spatially and temporally varying mole fraction of dissolved molecular water and hydroxyl, $X_{H_2O_m}$ and X_{OH} respectively, are calculated from the diffusion of H_2O_m and OH through the grain and across its surface into the nitrogen atmosphere of the TGA sample chamber. The resultant rate of change in total water content is thus given by

$$\frac{dX_{H_2O_t}}{dt} = \int_{r=0}^{R} \left[\frac{\partial X_{H_2O_m}}{\partial t} + \frac{1}{2} \frac{\partial X_{OH}}{\partial t} \right] dr, \quad (11)$$

where

$$\begin{cases} \dfrac{\partial X_{H_2O_m}}{\partial t} & = D_{H_2O_m}\left(\dfrac{\partial^2 X_{H_2O_m}}{\partial r^2}+\dfrac{2}{r}\dfrac{\partial X_{H_2O_m}}{\partial r}\right)-\dfrac{d\xi}{dt} \\ \dfrac{\partial X_{OH}}{\partial t} & = D_{OH}\left(\dfrac{\partial^2 X_{OH}}{\partial r^2}+\dfrac{2}{r}\dfrac{\partial X_{OH}}{\partial r}\right)+2\dfrac{d\xi}{dt} \end{cases}. \quad (12)$$

Here t denotes time, r is the radial coordinate ($0 \leqslant r \leqslant R$ with R being the radius of the grain), X indicates the mole fraction on a single oxygen basis (cf. Eqs. (3)–(5)), and $D_{H_2O_m}$ and D_{OH} are the diffusivities of H_2O_m and OH, respectively. The source term in Eq. (12), $d\xi/dt$, is the reaction rate of Eq. (1), given by (Zhang et al., 1997b) as

$$\frac{d\xi(r,t)}{dt} = k'_f X_{H_2O_m} X_O - k'_b X^2_{OH}. \quad (13)$$

$\xi(r, t)$ is the reaction progress parameter and $k'_f(r,t)$ and $k'_b(r,t)$ (s^{-1}) are the forward and backward reaction rate coefficients. According to Zhang et al. (1997b), the reaction rate coefficients depend on the 7th power of total water content. Eq. (13) can thus be rewritten as

$$\frac{d\xi(r,t)}{dt} = k_f X^7_{H_2O_t} X_{H_2O_m} X_O - k_b X^7_{H_2O_t} X^2_{OH}, \quad (14)$$

with $k_f = 1.010 \times 10^{33}\, e^{-42{,}620/T}\, s^{-1}$ and $k_b = 1.547 \times 10^{32}\, e^{-39{,}510/T}\, s^{-1}$ being temperature dependent, but independent on water content and speciation.

Because a repeated TGA of the same sample indicates that the samples have lost all their water by the end of the first TGA (cf. Section 3.7), we assume that the solubility at the outer margin of the grain can be approximated as a zero concentration Dirichlet boundary condition. Thus, the initial and boundary conditions for our model can be written, respectively, as

$$\begin{cases} X_{H_2O_m}(r,t) = X^{ini}_{H_2O_m} & \text{at } 0 \leqslant r \leqslant R \text{ and } t = 0, \\ X_{OH}(r,t) = X^{ini}_{OH} & \text{at } 0 \leqslant r \leqslant R \text{ and } t = 0, \end{cases} \quad (15)$$

$$\begin{cases} \frac{\partial X_{H_2O_m}}{\partial r} = 0 & \text{at } r = 0 \text{ and } t \geqslant 0, \\ \frac{\partial X_{OH}}{\partial r} = 0 & \text{at } r = 0 \text{ and } t \geqslant 0, \end{cases} \quad (16)$$

$$\begin{cases} X_{H_2O_m} = 0 & \text{at } r = R \text{ and } t > 0, \\ X_{OH} = 0 & \text{at } r = R \text{ and } t > 0 \end{cases}. \quad (17)$$

Here the initial mole fractions of H_2O_m and OH (i.e., $X^{ini}_{H_2O_m}$ and X^{ini}_{OH}) are calculated using Eqs. (3)–(5) with the water contents and speciation data measured by FTIR (cf. Table 4).

$D_{H_2O_m}$ is calculated using Eq. (8) (Zhang and Ni, 2010). Because there is no consistent formulation for $D_{H_2O_m}$ at temperatures <400 °C, we extrapolate Eq. (8) to room temperature. Furthermore, we assume that $D_{OH} = 0$, consistent with our current understanding of OH diffusion in silicates (cf. Zhang and Ni, 2010, and references therein). Nevertheless, even if $D_{OH} = 0$, the interconversion of OH to H_2O_m will eventually deplete the sample of OH.

We model individual grain sizes in increments of 0.5 μm across the full range of grain sizes ($0.5 \leqslant R \leqslant 26.5$ μm). For each grain size we solve Eqs. (11)–(14) and obtain the mass loss of the aggregate by summing the contribution of individual grain sizes across the particle size distribution of the sample aliquot obtained from image analysis.

5.3. Model results

We first present the results for a single sample and grain size, in order to describe the different processes occurring during the modeled TGA experiment (Section 5.3.1). We then explain the evolution of the modeled dTG profiles with grain sizes (Section 5.3.2). Lastly, we compare modeled and measured dTG profiles of three samples that represent typical end-member cases (Section 5.3.3).

In order to facilitate the presentation of our results, we define an instantaneous characteristic diffusion time of molecular water as $\tau_{D_m} \sim R^2/D_{H_2O_m}$ and $D_{H_2O_m}$ based on the volumetrically averaged concentrations of H_2O_t in each grain. In addition, we define the characteristic time for the speciation reaction, $\tau_\xi \sim X_{H_2O_m}/(-d\xi/dt)$, which is also based on the volumetrically averaged concentrations of H_2O_m and OH in each grain. Lastly, the constant characteristic heating time is $\tau_T \sim 10^3$ s.

5.3.1. Single grain size

Fig. 6 presents the model results for a 5 μm radius grain of sample G-1226 (4.38 wt% H_2O_t, 2.81 wt% H_2O_m, 1.57 wt% OH). The molecular water that was dissolved during sample hydration at magmatic conditions is lost at temperatures below approximately 450 °C (Fig. 6a). There is no noticeable OH loss over this temperature range because $D_{OH} \ll D_{H_2O_m}$.

As the temperature increases, the rate of conversion of OH to H_2O_m (i.e., $d\xi/dt$) increases. Above approximately 450 °C the conversion rate of OH to H_2O_m becomes similar to the diffusion rate of H_2O_m, in other words $\tau_\xi \sim \tau_{D_m}$ (Fig. 6b). From this point on, any OH that is converted to H_2O_m diffuses from the sample at the same rate at which it is being converted. If the conversion rate of OH to H_2O_m were faster than the diffusion rate of H_2O_m, the concentration of H_2O_m would increase relative to OH, resulting in a reduction in the conversion rate. Consequently, the diffusion of H_2O_m becomes rate limiting and τ_ξ becomes pegged to τ_{D_m}, with the concentration of H_2O_m remaining more or less constant. Furthermore, the gradual change in τ_ξ above approximately 450 °C is mostly caused by the Arrhenian dependence of $D_{H_2O_m}$ on temperature.

5.3.2. Influence of the grain size on the dTG curve

Fig. 7 illustrates the dependence on grain size, with one curve per grain size (0.5 μm in black, 5 μm in blue, 25 μm in magenta). For the same sample (G-1226), increasing grain radius, R, corresponds to an increase in τ_{D_m} (Fig. 7a). Consequently, the dTG peak associated with the diffusion of H_2O_m broadens and shift towards higher temperatures (Fig. 7b). In contrast, τ_ξ is independent of R and the dTG peak associated with the loss of OH, due to its conversion to H_2O_m and subsequent diffusion, is more or less fixed at approximately 550 °C (Fig. 7b). Fig. 7c shows the dTG curve for H_2O_t for each grain size, as well as the corresponding dTG curve for H_2O_t obtained by summing the contribution of all grain sizes across the particle size distribution of the sample (green curve). The shape of the dTG curve for the whole sample is largely controlled by the

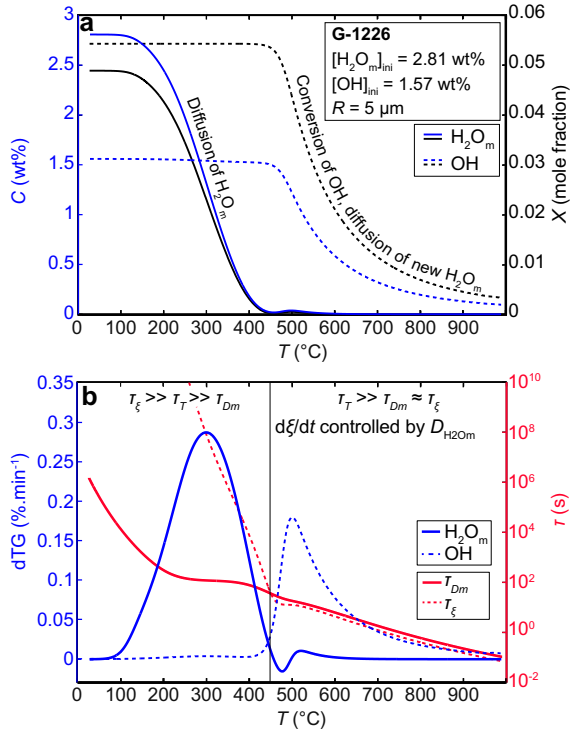

Fig. 6. Model results for a 5 μm-radius grain of sample G-1226 as a function of temperature, T. (a) Modeled concentration (C, blue) and mole fraction (X, black) of molecular water, H_2O_m, and hydroxyl, OH. (b) Mass loss of H_2O_m (dTG, thick blue), mass loss of OH (dTG, dashed blue), characteristic diffusion time of H_2O_m (τ_{D_m}, thick red), and characteristic reaction time (τ_ξ, dashed red). Diffusivity of molecular water, $D_{H_2O_m}$, increases with T. Above 100 °C, $\tau_{D_m} \lesssim \tau_T$ and mass loss due to diffusion of H_2O_m becomes noticeable. Between 200 and 400 °C the increase in $D_{H_2O_m}$, due to increasing T, is offset by decrease in $D_{H_2O_m}$, due to decreasing H_2O_m. Below 450 °C reaction rate $d\xi/dt$ increases, primarily due to decreasing H_2O_m. Above approximately 450 °C the concentration of H_2O_m approaches zero and the conversion rate of OH to H_2O_m becomes noticeable. Because the newly converted H_2O_m diffuses at a high rate, the concentration of H_2O_m remains close to zero despite the continuous conversion of OH to H_2O_m. (For interpretation of the references to color in this figure legend, the reader is referred to the web version of this article.)

largest grain sizes, because they represent the largest mass fraction of the sample (cf., Fig. 2b).

5.3.3. Modeled vs. measured dTG curves

Fig. 8 compares the modeled and measured dTG curves for three representative samples: G-1226 with approximately twice the amount of magmatic H_2O_m than OH, G-1300 with approximately twice the amount of magmatic OH than H_2O_m, and G-1290, which has few magmatic H_2O_m. The results of the other samples are intermediate to these three reference cases. Because we only model magmatic water, as determined by FTIR, the area below the modeled dTG curve is slightly lower than the measured one. Indeed, total water content measured by TGA is slightly higher than measured by FTIR (cf., Table 4), because adsorbed water is not analyzed by FTIR but it is by TGA.

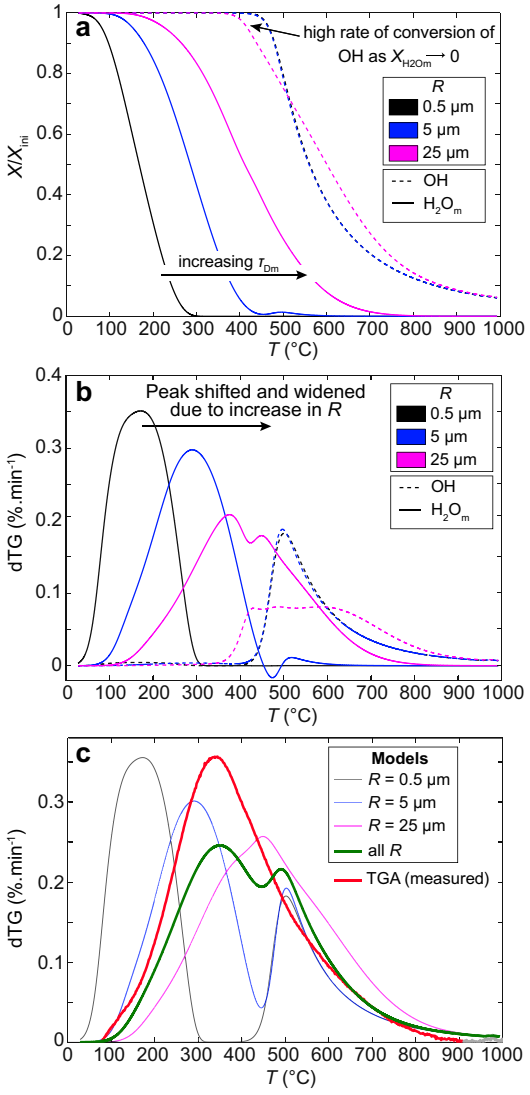

Fig. 7. Model results for three different grain sizes ($R = 0.5$, 5 and 25 μm) of sample G-1226 as a function of temperature, T. The blue curves ($R = 5$ μm) are the same blue curves as in Fig. 6b. (a) Variations in the mole fraction, X, of molecular water (H_2O_m, solid) and hydroxyl (OH, dashed), normalized to the initial mole fraction, X_{ini}. Loss of H_2O_m depends on the characteristic diffusion time, $\tau_{D_m} \sim R^2/D$, whereas loss of OH depends on the characteristic conversion rate τ_ξ. (b) Rate of mass loss, dTG, for H_2O_m (solid) and OH (dashed). The width and position of the peak for H_2O_m depend on τ_{D_m}, whereas the position of the peak in OH depends on τ_ξ. (c) Rate of mass loss, dTG, for the sum of H_2O_m and OH, that is H_2O_t. The presence of a single peak or two peaks depends on τ_{D_m}, which controls the width and position of the H_2O_m peak. The model result for the whole powder is shown in green and the measured dTG for sample G-1226 is shown in red. (For interpretation of the references to color in this figure legend, the reader is referred to the web version of this article.)

Overall, we find a reasonable agreement between modeled and measured dTG curves for the water-rich samples G-1226 and G-1300, but less for the water-poor sample G-1290. For sample G-1290 the model shows two distincts peaks related to the exsolution of H_2O_m at approximately 500 °C, and to the conversion of OH into H_2O_m and its

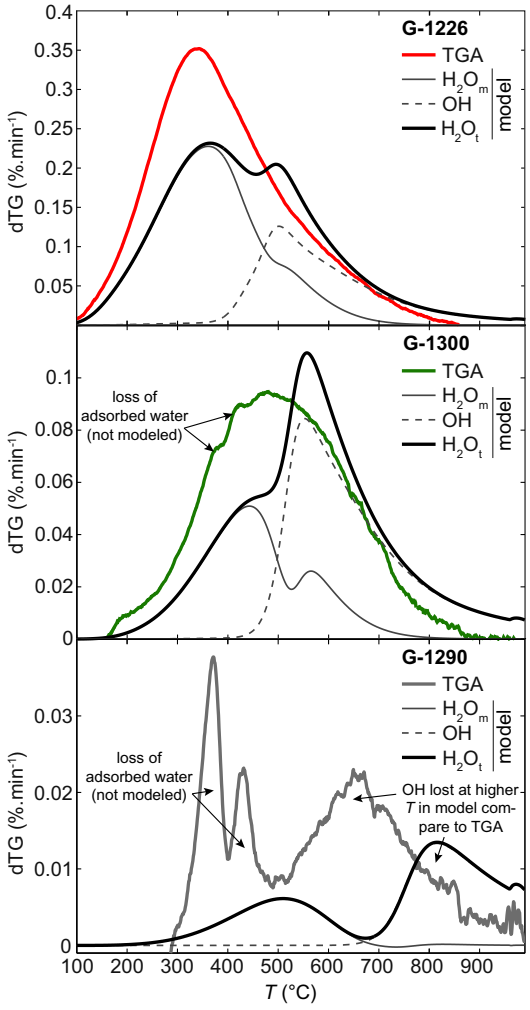

Fig. 8. Model results for three end-member cases (G-1226, G-1300, G-1290). Modeled dTG for molecular water (H_2O_m), hydroxyl (OH) and total water (H_2O_t) are shown together with the measured dTG. The loss of adsorbed water is modeled and, hence, the area below the modeled dTG is slightly lower than the area below the measured dTG. The model reproduces shift towards lower temperatures of magmatic water loss with increasing water content. For G-1290 the conversion of OH into H_2O_m and its diffusion occurs at higher temperatures than in the measured TGA. This suggests a non-negligible OH diffusivity at high temperatures and low water contents.

diffusion at approximately 820 °C. For samples G-1226 and G-1300, those two peaks are shifted to lower temperatures and somewhat overlap, forming a much broader peak which position roughly coincides with that measured. Our models thus reproduce the observed shift of the primary water peak(s) to lower temperatures with increasing water content, because of the decrease in τ_{D_m}.

6. DISCUSSION

6.1. Model sensitivity

Here we first illustrate the sensitivity of the model to the water diffusivity and to the rate of the speciation reaction. We then present the conditions for which the best fit of the model to the measured dTG curves is obtained. Model sensitivity on heating rate and sample geometry is also discussed in Appendices A and C, respectively.

The model results shown in Figs. 6–8 are based on the conservative assumption of negligible OH diffusion (i.e., $D_{OH} = 0$). However, Zhang et al. (1995) have suggested that, in addition to H_2O_m, OH may also diffuse in rhyolitic glass. Similarly, Ni et al. (2013) have suggested that D_{OH} may be finite and up to about one order of magnitude smaller than $D_{H_2O_m}$, at least under some conditions. Fig. 9 shows that a finite $D_{OH} \ll D_{H_2O_m}$ results in an improved fit of model predictions for samples with low water content (G-1290). The effect on more water-rich samples (G-1226 and G-1300) is less pronounced, but also leads to an improved fit by merging the two individual peaks into a single broader one. This result suggests that OH diffusion may not negligible in glasses with low magmatic water content, in other words, when water is mostly present as OH. The reaction rate used in this study has been calibrated to experiments between 398 and 549 °C (Zhang et al., 1997a). It is to our knowledge the only formulation for the reaction rate of water speciation in rhyolitic glass and to first order captures the kinetics of the speciation reaction. Fig. 9 illustrates that the model fit is improved for samples with low water if $d\xi/dt$ is allowed to be increased by up to a factor of 100, shifting the second peak to lower temperatures.

Fig. 10 shows that a good fit of the model to the data for all samples is obtained using $D_{OH}/D_{H_2O_m}$=1/20 and a $d\xi/dt$ five times higher than the value predicted by the formulation of Zhang et al. (1997a). Here, we also allowed the primary water content and relative proportion of OH and H_2O_m to vary within the errors associated with the FTIR measurements (Table 4, Fig. 10). Using the aforementioned modeling conditions and the grain size distribution of the analyzed sample, we can therefore predict the shape of the dTG curve associated with the loss of water of a rhyolitic glass, provided the dissolved water is magmatic.

6.2. Magmatic vs. secondary water

Recent studies suggest that secondary water in volcanic glasses, which consists predominantly or entirely of molecular water, is lost during TGA at temperatures below 550 °C, whereas magmatic water is lost above 550 °C (Roulia et al., 2006; Denton et al., 2012). It has also been suggested that the mass lost below 250 °C can be attributed to adsorbed water (Denton et al., 2012). Our models show that the temperature at which magmatic water is lost during TGA depends on grain size, water content of the sample and on heating rate (Appendix A). Consideration must also be given to water speciation and the diffusion of molecular water and perhaps also of hydroxyl. Overall, quantitative interpretation of TGA of volcanic glasses is improved by numerical modeling of water diffusion and speciation. Similarly, interpretation of K/Ar or ^{39}Ar/presup40Ar stepped heating data used in geochronology (e.g., Cosca and O'Nions, 1994; McDougall and Harrison, 1999; Kelley, 2002), was improved by numerical modeling of the temperature-dependent diffusion of argon in various

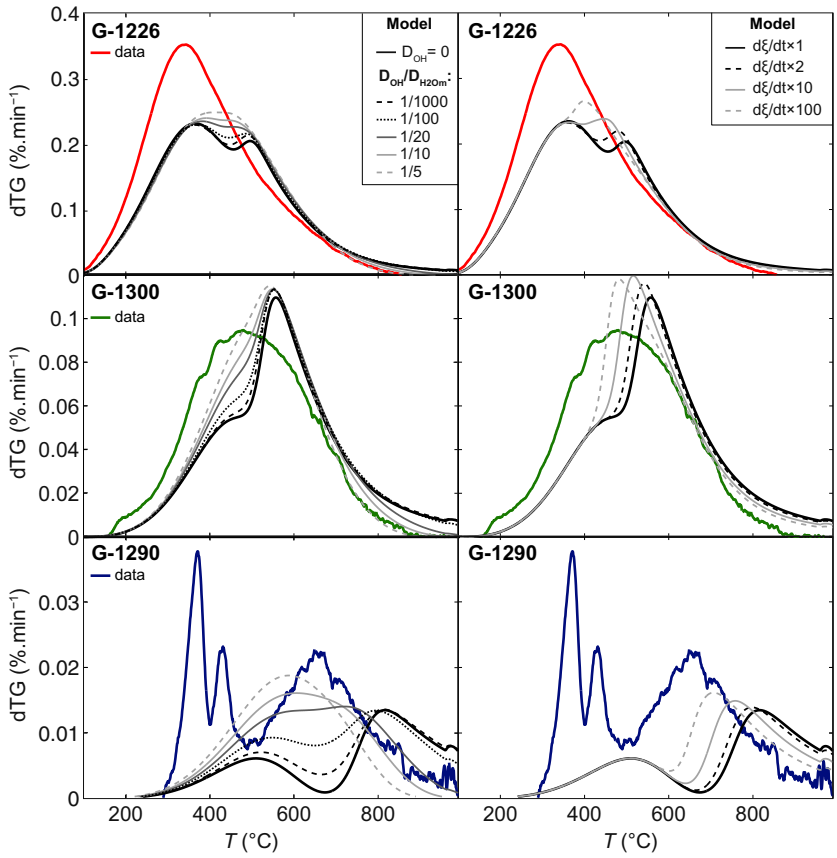

Fig. 9. Model sensitivity for D_{OH} (left column) and for $d\xi/dt$ (right column). Model fits are improved for $D_{OH} > 0$ (Ni et al., 2013), especially for samples with low water content (G-1290). Increasing $d\xi/dt$ leads to a shift of the second peak to lower temperatures, improving the fit, especially for water-poor samples.

glasses and minerals (e.g., Wheeler, 1996; Harrison et al., 2009).

7. MAGMATIC WATER IN GLASS MOUNTAIN PUMICES

The methodology previously developed is now applied to natural pumices in order to quantify their amount of magmatic water.

7.1. Samples

We collected nine Plinian fallout pumices from the explosive phase immediately preceding the emplacement of the 1060 CE Glass Mountain flow of Medicine Lake volcano, California (e.g., Anderson, 1933; Nathenson et al., 2007; Donnelly-Nolan et al., 2008), with the objective of quantifying the concentration of magmatic water retained in pumice during highly explosive eruptions. The bulk chemistry of these pumices is identical to that of the obsidian that was hydrated at magmatic conditions for subsequent TGA (e.g., Heiken, 1978). The volatile content other than water is negligible for these pumices (Eichelberger and Westrich, 1981). Pumice clasts vary in size from few centimeters to few decimeters and have a crystal content of approximately 3% (Tatlock et al., 1976). The volume fraction of vesicles was measured by He-pycnometry and varies from 0.69 to 0.81, with connected vesicle between 0.81 and 0.97. Because of the high connected porosity and an age of approximately 1000 years, these samples may contain a significant amount of secondary water.

7.2. TGA

During TGA of volcanic pyroclasts that have a high connected porosity, the distance over which water diffuses before being lost in the atmosphere of the TGA chamber is the half thickness of the matrix glass separating individual vesicles, which may be as low as <0.5 μm (e.g., Klug and Cashman, 1996; Giachetti et al., 2010). To illustrate this statement, we performed TGA on both (1) a 6–10 mm piece of the raw pumice and (2) the crushed pumice (grains of ≈10–20 μm, see Appendix B), for seven of the pumices collected, and using the procedure described in Section 3.7. Fig. 11a shows that the typical dTG curves obtained for the two different preparations of a single sample look very similar, despite the huge difference in the analyzed grain size (three orders of magnitude, see Appendix B). The powders lost 0.1–0.4% more mass than the corresponding raw pieces due to water adsorption before TGA by the new surface areas created by crushing. The shift to lower temperatures of the peaks observed on the dTG curves of

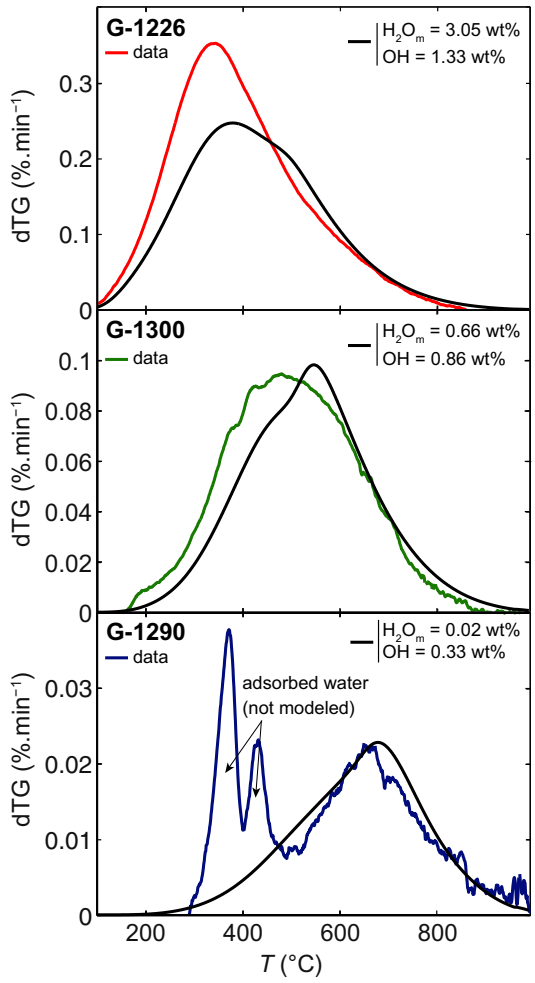

Fig. 10. A good fit of the model to the measured dTG curves is obtained with $D_{OH} \sim 0.05 \times D_{H_2O_m}$, $d\xi/dt$ is 5× the value of Zhang et al. (1997a) (Eqs. (13) and (14)), and initial primary water that are kept inside the errors associated with the FTIR values. The initial water content and speciation used for these 'best' models are provided in the legend of each sample.

the powders compare to those of the raw pieces (Fig. 11b) is explained by the reduction of the average diffusion length due to the breakage of some of the bubble walls during crushing. Overall, Fig. 11 illustrates that the shape of the dTG curve of highly vesicular samples is indeed primarily controlled by the vesicle wall thicknesses and not by the size of the grains analyzed. We therefore use the dTG curves of the raw pumices together with a bubble-wall thickness distribution in the model to discriminate magmatic from secondary/adsorbed water. The bubble-wall thickness distribution was obtained by analysis of SEM images taken at three different magnifications (×70, ×250 and ×1200) on a typical pumice (Fig. 12a), the minimum measurable thickness being 0.61 μm. Fig. 12b shows that the bubble-wall half thickness ranges from 0.65 to 27.8 μm and that the cumulative frequency distribution can be fitted by a third-degree polynomial.

The TGA of the Plinian Glass Mountain pumices yields water contents of 1.0–2.3 wt%, consistent with the values obtained by Eichelberger and Westrich (1981). Fig. 13a shows a major dTG peak around 315–355 °C and a second smaller peak around 650–700 °C, which is more (blue curve) or less (red curve) pronounced.

7.3. Numerical modeling of the dTG curves

To discriminate magmatic water in the Glass Mountain pumices we used the numerical model developed in Section 5 while assuming that the pumices were quenched at 850 °C to calculate the speciation of water in the matrix-glass, and using the bubble-wall half thickness size distribution shown in Fig. 12b. From the sensitivity analysis (Section 6.1), we also used $D_{OH}/D_{H_2O_m}$=1/20 and a $d\xi/dt$ five time higher than the value predicted by the formulation of Zhang et al. (1997a).

Modeling of the TGA clearly indicates that the water dissolved in the matrix-glass of these Plinian pumices cannot be only magmatic as the models do not fit the data at all (Fig. 13b). However, Fig. 13c shows that the peak at high temperature on the measured dTG curves can be

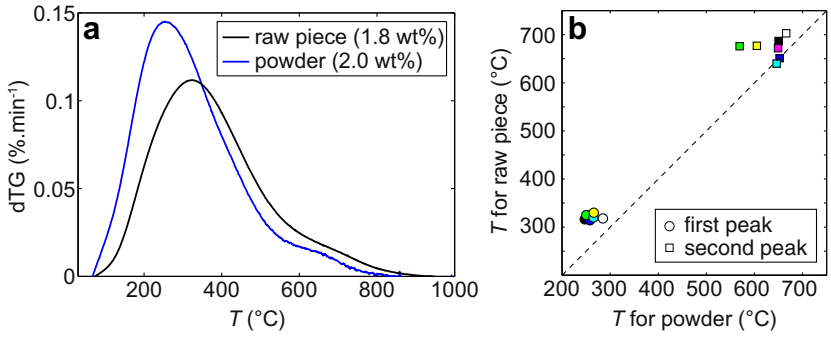

Fig. 11. (a) dTG curves for a un-crushed (black) and crushed (blue) Glass Mountain pumice. The 0.2 wt% difference in the total water contents of the powder and the whole piece is due to higher water adsorption before TGA by the powder. This is observed for all seven pumices that were analyzed following the two types of preparation (0.1–0.4 wt% difference). Note the overall similarity between the dTG curves, which have a large peak at 255 °C (powder) or 325 °C (whole) and a shoulder around 650–700 °C. (b) Temperatures of the first (circles) and second (square) peaks for several analyzes of powders and whole samples, demonstrating that the position of the peaks is controlled by the bubble wall thickness which also controls the grain size of crushed samples. (For interpretation of the references to color in this figure legend, the reader is referred to the web version of this article.)

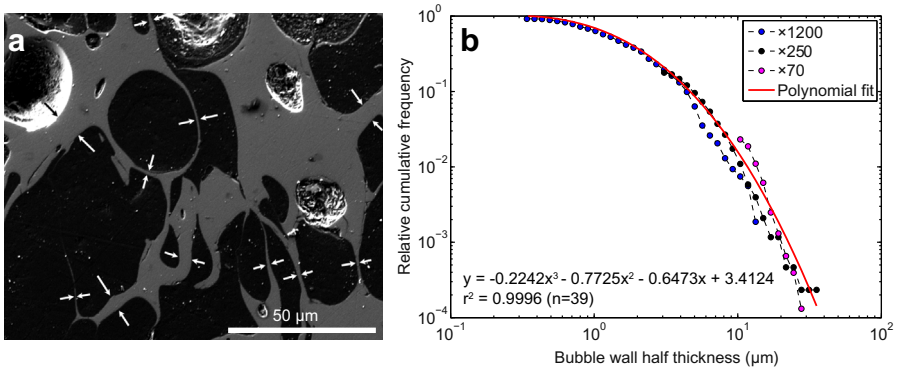

Fig. 12. (a) SEM image of a typical Plinian pumice (×1200 magnification). 1602 bubble wall thicknesses, as those highlighted between the arrows, were measured in total. Each thickness was at least 5 pixels. (b). Cumulative relative frequency distribution of bubble-wall half thickness. The third-degree polynomial fit of this distribution (red curve) was used in the numerical modeling of the dTG curves. (For interpretation of the references to colour in this figure legend, the reader is referred to the web version of this article.)

nicely fitted by assuming that the amount of primary water is only 0.20 (red) to 0.45 wt% (blue), the remaining 0.8–1.9 wt% thus being secondary (and also probably adsorbed) water, whose loss is not modeled. As shown in Appendix C, the geometry used to model the bubble wall does not impact this result. The magmatic water content of these Plinian pumices (0.20–0.45 wt%) is thus similar to that measured in the rhyolitic obsidian emitted after the Plinian phase (e.g., Eichelberger and Westrich, 1981; DeGroat-Nelson et al., 2001; Castro et al., 2005).

Given the bubble-wall thickness distribution we calculated and assuming that water solubility at atmospheric conditions is in the range 3–10 wt% (cf. Section 2.2), 0.8–1.9 wt% of secondary correspond to a rehydrated layer of 0.2–2.6 µm below the surface each bubble wall. Given the age of the sample (≈1000 years), a rehydrated layer of 0.2–2.6 µm would correspond to a diffusivity of water at atmospheric conditions of $10^{-24.1}$ to $10^{-21.7}$ $m^2 \cdot s^{-1}$, which is consistent with the diffusivities available in the literature (e.g., see Table 2 of Giachetti and Gonnermann, 2013).

7.4. Comparison with pyroclasts from other explosive eruptions

The Glass Mountain pumices contain only 0.2–0.5 wt% of residual magmatic water as demonstrated by our study, and the magma therefore had lost almost all of its dissolved magmatic water upon eruption as it initially contained around 4–6 wt% of magmatic water (Grove et al., 1997). This result is consistent with the low water contents measured in fresh (i.e., non-rehydrated) pumices from other highly explosive eruptions of silicic magma; 0.3 wt% in the 1991 Plinian pumices from Mount Pinatubo (Gerlach et al., 1996), <0.35 wt% in the pumices from the Plinian eruption of Cordón Caulle in 2011 (Castro et al., 2014).

Giachetti and Gonnermann (2013) showed that the relatively high water contents measured in pyroclasts from the Glass Mountain eruption, but also from other explosive eruptions as the 1997 Vulcanian explosions of Soufrière Hills (Burgisser et al., 2010), the 79 CE Plinian eruption of Vesuvius (Balcone-Boissard et al., 2008), the 1912 Plinian eruption of Novarupta (Giachetti and Gonnermann, 2013), or the 1350 CE Plinian eruption of Mount Pelée (Villemant and Boudon, 1999), can be explained solely by the rehydration, after the eruption, of a glass with a magmatic water close to 0. Our results show that it is the case for the Glass Mountain pumice, which was rehydrated with up to 2 wt% of water during the approximately 1000 years since the eruption. Together, those two studies strongly suggest that most pyroclasts from highly explosive eruptions are extensively degassed during eruption and rehydrated afterwards.

8. CONCLUSIONS

The degassing of magmatic water strongly affects the style and intensity of volcanic eruptions and measuring its final concentration in the erupted products helps putting constrains on its behavior during the eruption. Yet, the large amounts of water measured in pyroclasts from explosive eruptions may be the consequence of diffusive rehydration of the volcanic glass by meteoric water after the eruption. It is therefore essential to be able to discriminate between magmatic and secondary water in the matrix glass of these pyroclasts.

We used thermogravimetry to analyze the loss of water from rhyolitic glasses that were hydrated in the laboratory at magmatic temperatures and pressures. Numerical modeling of diffusive water loss during thermogravimetric analyses accounted for the diffusion of both H_2O_m and OH, and the interconversion of the two species. The model indicates that primary water is lost with increasing temperature through the diffusion of H_2O_m, the conversion of OH into H_2O_m and subsequent diffusion, as well as diffusion of OH at much smaller diffusivities than that of H_2O_m. The temperature at which the loss of primary water peaks during thermogravimetric analysis decreases with increasing total water content, decreasing grain size and decreasing heating rate. This feature does not allow for the discrimination of magmatic and secondary water using a simple temperature threshold criterion, but rather encourages the integration of thermogravimetric analysis and numerical

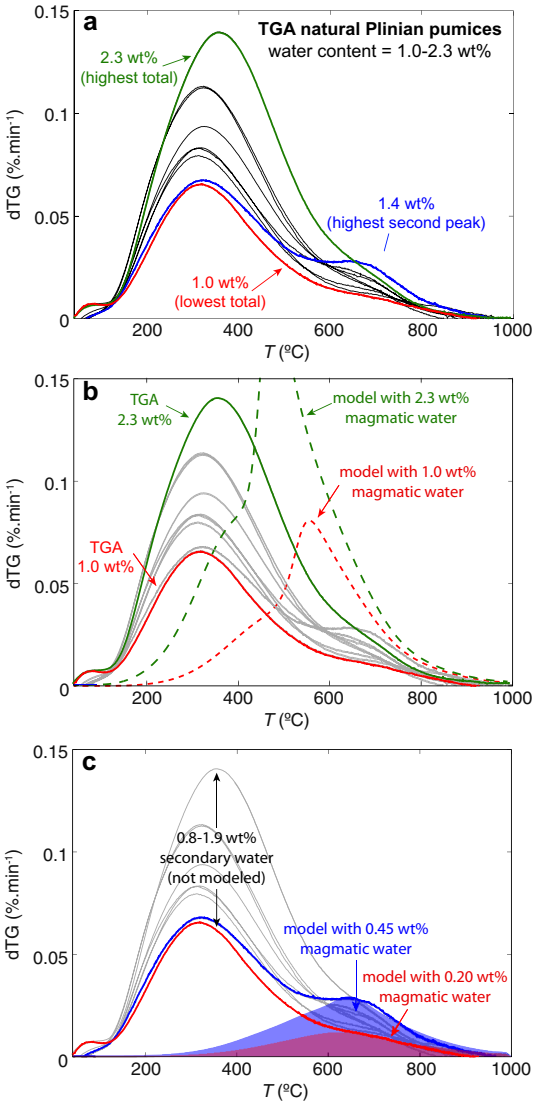

Fig. 13. (a) Measured dTG curves of nine natural pumices from Glass Mountain eruption. The total mass loss ranges from 1.0% (red curve) to 2.3% (green curve). The dTG are very similar, with a major peak around 315–355 °C and another peak/shoulder around 650–700 °C. The sample symbolized by the blue curve was used to perform the bubble-wall thickness distribution. It has also the highest second peak around 700 °C. (b) Modeled dTG obtained assuming that the water measured by TGA is only magmatic (red and green dashed curves) do not reproduce the data (red and green solid curves) at all. (c) Modeled dTG obtained assuming that the sample contains 0.20 (red area) to 0.45 wt% (blue area) of magmatic water fit the second peak of the measured dTG curves (red and blue). The remaining 0.8–1.9 wt% of water, which is lost around 315–355 °C, is secondary water (with minor adsorbed water), not modeled. For (b) and (c) modeled dTG were obtained assuming $D_{OH}/D_{H_2O_m}=1/20$ and $d\xi/dt$ is five times the value of Zhang et al. (1997a), as suggested by the sensitivity analysis (Section 6.1). (For interpretation of the references to color in this figure legend, the reader is referred to the web version of this article.)

modeling to facilitate the distinction between the magmatic and secondary water content of volcanic glasses.

Application of our model to natural pumices from the Plinian phase of the 1060 CE Glass Mountain eruption indicates that these pyroclasts contain only 0.2–0.5 wt% of magmatic water, but gained 1–2 wt% of atmospheric water by diffusive rehydration during the past 950 years. These results confirm that the majority of magmatic water was lost from the magma during this Plinian eruption. We suggest that Plinian pumices elsewhere may also become largely degassed during the eruption, an inference that should be confirmed through more thorough analysis of magmatic water contents in pyroclasts from highly explosive eruptions. Overall, our results emphasize the likely importance of open-system degassing during explosive volcanic eruptions and motivates further research to quantify this process.

ACKNOWLEDGEMENTS

We thank C.A. Masiello and R. Dasgupta who gave us access to their laboratories and S. Kohl for his help in restoring the Q500. This paper greatly benefited from the thorough reviews by H.M.N. Wright, H. Tuffen and I.N. Bindeman and by the Associate editor L.M. Anovitz. T.G. and H.M.G. were in part supported by NSF grants EAR-1250451, EAR-1348072 and CMMI-1015069. Any opinions, findings, and conclusions or recommendations expressed in this material are those of the authors and do not necessarily reflect the views of the National Science Foundation.

APPENDIX A. MODEL SENSITIVITY TO HEATING RATE

We modeled the dTG curve for a grain 50 microns in diameter with the primary water content of sample G-1226. We ran the model for three different heating rates (0.1, 1 and 5 °C·min^{-1}), in addition to that used in our study (20 °C·min^{-1}). Fig. A.1 shows that decreasing the heating rate leads to a shift of the peaks to lower temperature, especially that associated with the diffusion of the initial H_2O_m. This is due to an increase of the characteristic time for the heating, τ_T, which reaches up to $\sim 10^6$ s when using a heating rate of 0.1 °C·min^{-1}. It leads to a decrease of the temperature at which $\tau_{D_m} < \tau_T$. Note, that this effect is partly similar to that obtained when keeping the heating rate constant, but decreasing the grain size (compare Fig. A.1 with Fig. 7c.).

APPENDIX B. PARTICLE SIZE DISTRIBUTION OF THE NATURAL PUMICES

The pieces of raw natural pumices analyzed by thermogravimetry had an initial mass of 70 to 245 mg. Assuming a density of the solid fraction of 2.43 g·cm^{-3}, a vesicularity of 69–81% and spherical geometry, the raw pieces have a radius of approximately 2700–5000 μm.

The particle size distributions of five of the powdered pumices were obtained using a Malvern Mastersizer 2000 laser particle size analyzer. A refractive index of 1.507 was used, calculated using the formulation of Church and Johnson (1980) and the glass chemistry obtained by EMP (cf., Table 3), assuming the bulk chemistry of the obsidian

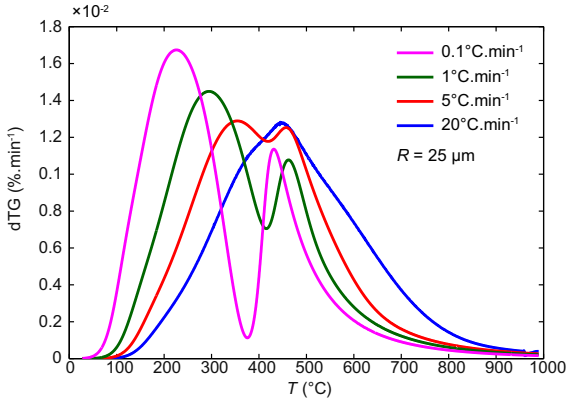

Fig. A.1. Impact of varying the heating rate used on the shape of the modeled dTG curve for a grain of 50 µm and the initial water content of sample G-1226. The blue curve is the same as the blue curve in Fig. 7c. (For interpretation of the references to color in this figure legend, the reader is referred to the web version of this article.)

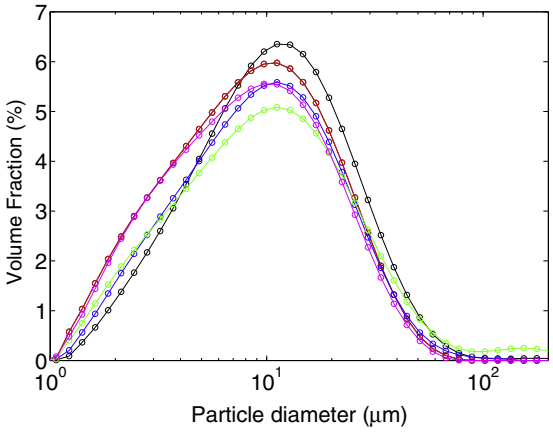

Fig. B.1. Particle size distribution of five of the powdered BGM pumices.

and the pumices from Glass Mountain eruption is the same (Heiken, 1978). The powdered pumices were thoroughly mixed with deionized water before analysis. The particle size distributions of the five samples are similar (cf., Fig. B.1), exhibiting a Gaussian distribution with a unique peak around 10–15 µm. The largest particles measured in all five powders are ≈100 µm. The particle size distributions of the other samples were considered to be equal to the average of the five distributions presented here.

For each sample, the piece of raw pumice analyzed is therefore roughly three orders of magnitude larger than the average grain size of the powder.

APPENDIX C. MODEL SENSITIVITY TO GEOMETRY

We modeled the dTG curve of one natural pumice with a primary water content of 0.45 wt%, the water speciation at a magmatic temperature of 850 °C, and using three

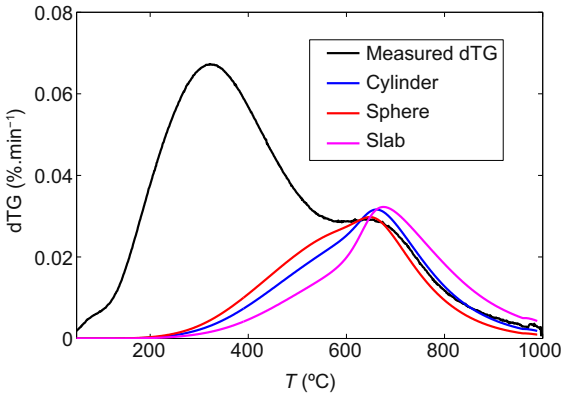

Fig. C.1. Modeled dTG curves as a function of the geometry used to model the wall between individual vesicles. The measured dTG curve is plotted for comparison.

different geometries for the bubble wall: sphere, cylinder, slab. In the three cases, the model was first run for fifty characteristic diffusion lengths (i.e., radius of the sphere or of the cylinder, half thickness of the slab) from 0.3 to 40 microns, and the resulting dTG curves then combined following the cumulative frequency distribution calculated by image analysis and presented in Fig. 12b. Fig. C.1 shows that the geometry used to model the wall between individual vesicles impacts only slightly the result. In all three cases, the model reproduces well the second peak visible on the measured dTG curve.

REFERENCES

Anderson C. A. (1933) Volcanic history of Glass Mountain, northern California. *Am. J. Sci.* **5**, 485–506.

Anovitz L. M., Elam M., Riciputi L. and Cole D. (1999) The failure of obsidian hydration dating: Sources, implications, and new directions. *J. Archeol. Sci.* **26**, 735–752.

Anovitz L. M., Cole D. R. and Fayek M. (2008) Mechanisms of rhyolitic glass hydration below the glass transition. *Am. Mineral.* **93**, 1166–1178.

Applegarth L. P., Tuffen H., James M. R. and Pinkerton H. (2013) Degassing-driven crystallisation in basalts. *Earth Sci. Rev.* **116**, 1–16.

Bagdassarov N. and Dingwell D. (1994) Thermal properties of vesicular rhyolite. *J. Volcanol. Geotherm. Res.* **60**, 179–191.

Balcone-Boissard H., Villemant B., Boudon G. and Michel A. (2008) Non-volatile vs. volatile behaviours of halogens during the AD 79 Plinian eruption of Mt. Vesuvius, Italy. *Earth Planet. Sci. Lett.* **269**, 66–79.

Burgisser A., Poussineau S., Arbaret L., Druitt T., Giachetti T. and Bourdier J. (2010) Pre-explosive conduit conditions of the 1997 Vulcanian explosions at Soufriere Hills Volcano, Montserrat: I. Pressure and vesicularity distributions. *J. Volcanol. Geotherm. Res.* **194**, 27–41.

Burnham C. W. (1979) Magmas and hydrothermal fluids. In *Geochemistry of Hydrothermal Ore Deposits* (ed. H. Barnes). Wiley, New York, pp. 71–136.

Cashman K. V. (2004) Volatile controls on magma ascent and eruption. In *The State of the Planet: Frontiers and Challenges in Geophysics: Geophysical Monograph 150* (eds. R. S. J. Sparks and C. J. Hawkesworth). Carnegie Inst. Wash Publ., Washington, D.C. American Geophysical Union.

Castro J. M., Manga M. and Martin M. C. (2005) Vesiculation rates of obsidian domes inferred from H_2O concentration profiles. *Geophys. Res. Lett.* **32**, L21307.

Castro J. M., Bindeman I. N., Tuffen H. and Schipper C. I. (2014) Explosive origin of silicic lava: Textural and $\delta D?H_2O$ evidence for pyroclastic degassing during rhyolite effusion. *Earth Planet. Sci. Lett.* **405**, 52–61.

Cherniak D. J., Hervig R., Koepke J., Zhang Y. and Zhao D. (2010) Analytical methods in diffusion studies. *Rev. Mineral. Geochem.* **72**, 107–170.

Christy A. A. (2010) New insights into the surface functionalities and adsorption evolution of water molecules on silica gel surface: A study by second derivative near infrared spectroscopy. *Vib. Spectrosc.* **54**, 42–49.

Church B. N. and Johnson W. M. (1980) Calculation of the refractive index of silicate glasses from chemical composition. *Geol. Soc. Am. Bull.* **91**, 619–625.

Cosca M. A. and O'Nions R. K. (1994) A re-examination of the influence of composition on argon retentivity in metamorphic calcic amphiboles. *Chem. Geol.* **112**, 39–56.

DeGroat-Nelson P. J., Cameron B. I., Fink J. H. and Holloway J. R. (2001) Hydrogen isotope analysis of rehydrated silicic lavas: Implications for eruption mechanisms. *Earth Planet. Sci. Lett.* **185**, 331–341.

Delmelle P., Villiéras F. and Pelletier M. (2005) Surface area, porosity and water adsorption properties of fine volcanic ash particles. *Bull. Volcanol.* **67**, 160–169.

Denton J. S., Tuffen H., Gilbert J. S. and Odling N. (2009) The hydration and alteration of perlite and rhyolite. *J. Geol. Soc. London* **166**, 895–904.

Denton J. S., Tuffen H., Gilbert J. S. and Odling N. (2012) Variations in hydration within perlitised rhyolitic lavas-evidence from Torfajökull, Iceland. *J. Volcanol. Geotherm. Res.*, 64–73.

Deubener J., Muller R., Behrens H. and Heide G. (2003) Water and the glass transition temperature of silicate melts. *Non-crystalline Solids* **330**, 268–273.

Dingwell D. B., Romano C. and Hess K.-U. (1996) The effect of water on the viscosity of a haplogranitic melt under P–T–X conditions relevant to silicic volcanism. *Contrib. Mineral. Petrol.* **124**, 19–28.

Donnelly-Nolan J. M., Grove T. L., Lanphere M. A., Champion D. E. and Ramsey D. W. (2008) Eruptive history and tectonic setting of Medicine Lake Volcano, a large rear-arc volcano in the southern Cascades. *J. Volcanol. Geotherm. Res.* **177**, 313–328.

Duan X. (2014) A general model for predicting the solubility behavior of H_2O–CO_2 fluids in silicate melts over a wide range of pressure, temperature and compositions. *Geochim. Cosmochim. Acta* **125**, 582–609.

Eichelberger J. C. (1995) Silicic volcanism: Ascent of viscous magmas from crustal reservoirs. *Annu. Rev. Earth Planet. Sci.* **23**, 41–63.

Eichelberger J. and Westrich H. (1981) Magmatic volatiles in explosive rhyolitic eruptions. *Geophys. Res. Lett.* **8**, 757–760.

Friedman I. and Long W. (1976) Hydration rate of obsidian. *Science* **191**, 347–352.

Friedman I., Long W. and Smith R. L. (1963) Viscosity and water content of rhyolitic glass. *J. Geophys. Res.* **68**, 6523–6535.

Friedman I., Smith R. and Long W. (1966) Hydration of natural glass and formation of perlite. *Geol. Soc. Am. Bull.* **77**, 323–328.

Gardner J. E., Thomas R. M. E., Jaupart C. and Tait S. (1996) Fragmentation of magma during Plinian volcanic eruptions. *Bull. Volcanol.* **58**, 144–162.

Gardner J. E., Hilton M. and Carroll M. R. (1999) Experimental constraints on degassing of magma: Isothermal bubble growth during continuous decompression from high pressure. *Earth Planet. Sci. Lett.* **168**, 201–208.

Gardner J. E., Hilton M. and Carroll M. R. (2000) Bubble growth in highly viscous silicate melts during continuous decompression from high pressure. *Geochim. Cosmochim. Acta* **64**, 1473–1483.

Garofalini S. H. (1990) Molecular dynamics computer simulations of silica surface structure and adsorption of water molecules. *J. Non-cryst. Solids* **120**, 1–12.

Gerlach T. M., Westrich H. R. and Symonds R. B. (1996) Pre-eruption vapor in magma of the climactic Mount Pinatubo eruption: Source of the giant stratospheric sulfur dioxide cloud. In *Fire and Mud: Eruptions and Lahars of Mount Pinatubo, Philippines* (eds. C. G. Newhall and R. Punongbayan). University of Washington Press, Seattle, pp. 415–433.

Giachetti T. and Gonnermann H. M. (2013) Water in volcanic pyroclast: Rehydration or incomplete degassing? *Earth Planet. Sci. Lett.*, 317–332.

Giachetti T., Druit T., Burgisser A., Arbaret L. and Galven C. (2010) Bubble nucleation, growth and coalescence during the 1997 Vulcanian explosions of Soufrire Hills Volcano, Montserrat. *J. Volcanol. Geotherm. Res.* **193**, 215–231.

Giordano D. and Dingwell D. B. (2003) Non-Arrhenian multicomponent melt viscosity: A model. *Earth Planet. Sci. Lett.* **208**, 337–349.

Goff F. and McMurtry G. M. (2000) Tritium and stable isotopes of magmatic waters. *J. Volcanol. Geotherm. Res.* **97**, 347–396.

Gonnermann H. M. and Houghton B. F. (2012) Magma degassing and fragmentation during the Plinian eruption of Novarupta, Alaska, 1912. *G-cubed* **13**, Q10009.

Gonnermann H. M. and Manga M. (2007) The fluid mechanics inside a volcano. *Annu. Rev. Fluid Mech.* **39**, 321–356.

Goranson R. W. (1931) The solubility of water in granite magmas. *Am. J. Sci.* **22**, 481–502.

Grove T. L. and Donnelly-Nolan J. M. (1986) The evolution of young silicic lavas at Medicine Lake Volcano, California: Implications for the origin of compositional gaps in calc-alkaline series lavas. *Contrib. Mineral. Petrol.* **92**, 281–302.

Grove T. L., Donnelly-Nolan J. M. and Housh T. (1997) Magmatic processes that generated the rhyolite of Glass Mountain, Medicine Lake volcano, N. California. *Contrib. Mineral. Petrol.* **127**, 205–223.

Harford C., Sparks R. and Fallick A. (2003) Degassing at the Soufrire Hills Volcano, Montserrat, recorded in matrix glass compositions. *J. Petrol.* **44**, 1503–1523.

Harrison T. M., Célérier J., Aikman A. B., Hermann J. and Heizler M. T. (2009) Diffusion of ^{40}Ar in muscovite. *Geochim. Cosmochim. Acta* **73**, 1039–1051.

Heiken G. (1978) Plinian-type eruptions in the Medicine Lake Highland, California, and the nature of the underlying magma. *J. Volcanol. Geotherm. Res.* **4**, 375–402.

Holtz F., Behrens H., Dingwell D. B. and Taylor R. P. (1995) H_2O solubility in haplogranitic melts: Compositional, pressure, and temperature dependence. *Am. Mineral.* **80**, 94–108.

Hui H., Zhang Y., Xu Z. and Behrens H. (2008) Pressure dependence of the speciation of dissolved water in rhyolitic melts. *Geochim. Cosmochim. Acta* **72**, 3229–3240.

Hurwitz S. and Navon O. (1994) Bubble nucleation in rhyolite melts: Experiments at high pressure, temperature, and water content. *Earth Planet. Sci. Lett.* **122**, 267–280.

Ihinger P. D., Hervig R. L. and McMillan P. F. (1994) Analytical methods for volatiles in glasses. *Rev. Mineral. Geochem.* **30**, 67–121.

Jarosewich E., Nelen J. A. and Norberg J. A. (1980) Reference samples for electron microprobe analysis. *Geostand. Newsletter* **4**, 43–47.

Jaupart C. and Allègre C. J. (1991) Gas content, eruption rate and instabilities of eruption regime in silicic volcanoes. *Earth Planet. Sci. Lett.* **102**, 413–429.

Jezek P. A. and Noble D. C. (1978) Natural hydration and ion exchange of obsidian: An electron microprobe study. *Am. Mineral.* **63**, 266–273.

Kelley S. (2002) Excess argon in K–Ar and Ar–Ar geochronology. *Chem. Geol.* **188**, 1–22.

Klug C. and Cashman K. V. (1996) Permeability development in vesiculating magmas: Implications for fragmentation. *Bull. Volcanol.* **58**, 87–100.

Kunkel W. B. (1950) The static electrification of dust particles on dispersion into a cloud. *J. Appl. Phys.* **21**, 820.

Leal O., Bolivar C., Ovalles C., Garcia J. J. and Espidel Y. (1995) Reversible adsorption of carbon dioxide on amine surface-bonded silica gel. *Inorg. Chim. Acta* **240**, 183–189.

Lee R. R., Leich D. A., Tombrello T. A., Ericson J. E. and Friedman I. (1974) Obsidian hydration profile measurements using a nuclear reaction technique. *Nature* **250**, 44–47.

Liritzis I. and Laskaris M. (2011) Fifty years of obsidian hydration dating in archaeology. *J. Non-crys. Solids* **357**, 2011–2023.

Liu Y., Zhang Y. and Behrens H. (2005) Solubility of H_2O in rhyolitic melts at low pressures and a new empirical model for mixed H_2O–CO_2 solubility in rhyolitic melts. *J. Volcanol. Geotherm. Res.* **143**, 219–235.

Lyakhovsky V., Hurwitz S. and Navon O. (1996) Bubble growth in rhyolitic melts: Experimental and numerical investigation. *Bull. Volcanol.* **58**, 19–32.

McDougall I. and Harrison T. M. (1999) *Geochronology and Thermochronology by the $^{40}Ar/^{39}Ar$ Method*. Oxford University Press, New York.

McIntosh I. M., Llewellin E. W., Humphreys M. C. S., Nichols A. R. L., Burgisser A., Schipper C. I. and Larsen J. F. (2014) Distribution of dissolved water in magmatic glass records growth and resorption of bubbles. *Earth Planet. Sci. Lett.* **401**, 1–11.

Moore G., Vennemann T. and Carmichael I. S. E. (1995) The solubility of water in natural silicate melts to 2 kilobars. *Geology* **23**, 1009–1102.

Namiki A. and Manga M. (2008) Transition between fragmentation and permeable outgassing of low viscosity magmas. *J. Volcanol. Geotherm. Res.* **169**, 48–60.

Nathenson M., Donnelly-Nolan J. M., Champion D. E. and Lowenstern J. B. (2007) Chronology of postglacial eruptive activity and calculation of eruption probabilities for Medicine Lake volcano, Northern California. *U.S. Geol. Surv. Sci. Inv. Rept.* **5174-B**, 10.

Newman S., Stolper E. M. and Epstein S. (1986) Measurement of water in rhyolitic glasses: Calibration of an infrared spectroscopic technique. *Am. Mineral.* **71**, 1527–1541.

Ni H. and Zhang Y. (2008) H_2O diffusion models in rhyolitic melt with new high pressure data. *Chem. Geol.* **250**, 68–78.

Ni H., Xu Z. and Zhang Y. (2013) Hydroxyl and molecular H_2O diffusivity in a haploandesitic melt. *Geochim. Cosmochim. Acta* **103**, 36–48.

Nolan G. S. and Bindeman I. (2013) Experimental investigation of rates and mechanisms of isotope exchange (O, H) between volcanic ash and isotopically-labeled water. *Geochim. Cosmochim. Acta* **111**, 5–27.

Okumura S. and Nakashima S. (2005) Molar absorptivities of OH and H_2O in rhyolitic glass at room temperature and at 400–600 °C. *Am. Mineral.* **90**, 441–447.

Okumura S., Nakamura M. and Nakashima S. (2003) Determination of molar absorptivity of IR fundamental OH-stretching vibration in rhyolitic glasses. *Am. Mineral.* **88**, 1657–1662.

Proussevitch A. A., Sahagian D. L. and Anderson A. T. (1998) Dynamics of diffusive bubble growth in magmas: Isothermal case. *J. Geophys. Res.* **98**, 22283–22307.

Razouk R. I. and Salem A. S. (1948) The adsorption of water vapor on glass surfaces. *J. Phys. Chem.* **52**, 1208–1227.

Richet P., Lejeune A. M., Holtz F. and Roux J. (1996) Water and the viscosity of andesite melts. *Chem. Geol.* **128**, 185–197.

Ross C. and Smith R. (1955) Water and other volatiles in volcanic glasses. *Am. Mineral.* **40**, 1071–1089.

Roulia M., Chassapis K., Kapoutsis J., Kamitsos E. and Savvidis T. (2006) Influence of thermal treatment on the water release and the glassy structure of perlite. *J. Mater. Sci.* **41**, 5870–5881.

Shaw H. R. (1972) Viscosities of magmatic silicate liquids: an empirical method of prediction. *Am. J. Sci.* **272**, 870–893.

Shaw H. R. (1974) Diffusion of H_2O in granitic liquids, I: Experimental data; II: Mass transfer in magma chambers. In *Geochemical Transport and Kinetics* (eds. A. Hofmann, B. Giletti, H. Yoder and R. Yund). Carnegie Inst. Wash Publ., Washington.

Sodeyama K., Sakka Y. and Kamino Y. (1999) Preparation of fine expanded perlite. *J. Mat. Sci.* **34**, 2461–2468.

Sparks R. S. J. (1978) The dynamics of bubble formation and growth in magmas. *J. Volcanol. Geotherm. Res.* **3**, 1–37.

Sparks R. S. J. (2003) Dynamics of magma degassing. *Geol. Soc. Lond. Spec. Pub.* **213**, 5–22.

Stevenson R. J., Dingwell D. B., Webb S. L. and Sharp T. G. (1996) Viscosity of microlite-bearing rhyolitic obsidians: An experimental study. *Bull. Volcanol.* **58**, 298–309.

Stevenson J. A., Smellie J. S., McGarvie D., Gilbert J. S. and Cameron B. (2009) Subglacial intermediate volcanism at Kerlingarfjll, Iceland: Magmawater interactions beneath thick ice. *J. Volcanol. Geotherm. Res.* **185**, 337–351.

Stolper E. (1982a) The speciation of water in silicate melts. *Geochim. Cosmochim. Acta* **46**, 2609–2620.

Stolper E. (1982b) Water in silicate glasses: An infrared spectroscopic study. *Contrib. Mineral. Petrol* **81**, 1–17.

Tatlock D. B., Flanagan F. J., Bastron H., Berman S. and Sutton Jr. A. L. (1976) Rhyolite, RGM-1, from Glass Mountain, California. In: *Descriptions and Analyses of Eight New USGS Rock Standards*. U.S. Geol. Surv., Prof. Pap. pp. 11–14.

Thomas N., Jaupart C. and Vergniolle S. (1994) On the vesicularity of pumice. *J. Geophys. Res.* **99**, 15633–15644.

Tuffen H., Owen J. and Denton J. S. (2010) Magma degassing during subglacial eruptions and its use to reconstruct palaeo-ice thicknesses. *Earth Sci. Rev.* **99**, 1–18.

Villemant B. and Boudon G. (1999) H_2O and halogen (F, Cl, Br) behaviour during shallow magma degassing processes. *Earth Planet. Sci. Lett.* **168**, 271–286.

Watkins J. M., Manga M. and DePaolo D. J. (2012) Bubble geobarometry: A record of pressure changes, degassing, and regassing at Mono Craters, California. *Geology* **40**, 699–702.

Westrich H. R. (1987) Determination of water in volcanic glasses by Karl-Fischer titration. *Chem. Geol.* **63**, 335–340.

Westrich H. R. and Eichelberger J. C. (1994) Gas transport and bubble collapse in rhyolitic magma: An experimental approach. *Bull. Volcanol.* **56**, 447–458.

Wheeler J. (1996) DIFFARG: A program for simulating argon diffusion profiles in minerals. *Comput. Geosci.* **22**, 919–929.

Withers A. C. and Behrens H. (1999) Temperature-induced changes in the NIR spectra of hydrous albitic and rhyolitic glasses between 300 and 100 K. *Phys. Chem. Minerals* **27**, 119–132.

Yoshimura S. and Nakamura M. (2008) Diffusive dehydration and bubble resorption during open-system degassing of rhyolitic melts. *J. Volcanol. Geotherm. Res.* **178**, 72–80.

Yoshimura S. and Nakamura M. (2010) Chemically driven growth and resorption of bubbles in a multivolatile magmatic system. *Chem. Geol.* **276**, 18–28.

Zhang Y. and Ni H. (2010) Diffusion of H, C, and O components in silicate melts. *Rev. Mineral. Geochem.* **72**, 171–225.

Zhang Y., Stolper E. M. and Wasserburg G. J. (1991) Diffusion of water in rhyolitic glasses. *Geochim. Cosmochim. Acta* **55**, 441–456.

Zhang Y., Stolper E. M. and Ihinger P. D. (1995) Kinetics of the reaction $H_2O + O = 2OH$ in rhyolitic and albitic glasses: Preliminary results. *Am. Mineral.* **80**, 593–612.

Zhang Y., Belcher R., Ihinger P. D., Wang L., Xu Z. and Newman S. (1997a) New calibration of infrared measurement of dissolved water in rhyolitic glasses. *Geochim. Cosmochim. Acta* **61**, 3089–3100.

Zhang Y., Jenkins J. and Xu Z. (1997b) Kinetics of the reaction $H_2O + O \leftrightharpoons 2OH$ in rhyolitic glasses upon cooling: Geospeedometry and comparison with glass transition. *Geochim. Cosmochim. Acta* **61**, 2167–2173.

Zhang Y., Stolper E. M. and Wasserburg G. J. (2000) Hydrous species geospeedometer in rhyolite: Improved calibration and application. *Geochim. Cosmochim. Acta* **64**, 3347–3355.

Zhang Y., Xu Z., Zhu M. and Wang H. (2007) Silicate melt properties and volcanic eruptions. *Rev. Geophys.* **45**, RG4004.

Associate editor: Lawrence M. Anovitz